

Importance of Diurnal Forcing on the Summer Salinity Variability in the East China Sea

YANG YU,^{a,b,c} SHU-HUA CHEN,^c YU-HENG TSENG,^d XINYU GUO,^{a,e} JIE SHI,^{a,b} GUANGLIANG LIU,^f
CHAO ZHANG,^a YI XU,^g AND HUIWANG GAO^{a,b}

^a Key Laboratory of Marine Environment and Ecology, Ministry of Education of China, Ocean University of China, Qingdao, China

^b Laboratory for Marine Ecology and Environmental Sciences, Qingdao National Laboratory for Marine Science and Technology, Qingdao, China

^c Department of Land, Air, and Water Resources, University of California, Davis, Davis, California

^d Institute of Oceanography, National Taiwan University, Taipei, Taiwan

^e Center for Marine Environmental Studies, Ehime University, Matsuyama, Japan

^f Qilu University of Technology (Shandong Academy of Sciences), Shandong Computer Science Center (National Supercomputer Center in Jinan), Shandong Provincial Key Laboratory of Computer Networks, Jinan, China

^g State Key Lab of Marine Environmental Science, College of Ocean and Earth Sciences, Xiamen University, Xiamen, China

(Manuscript received 16 August 2019, in final form 1 January 2020)

ABSTRACT

The impacts of diurnal atmospheric forcing on the summer salinity change in the East China Sea are investigated using the Regional Ocean Modeling System, forced by the hourly and daily reanalysis of wind and insolation. The differences between the forcing of these two frequencies reveal a dipole pattern of salinity change with a positive salinity deviation (1–2 psu) offshore of the Yangtze River estuary, and a negative deviation (from –1 to –0.5 psu) along the Jiangsu Coast. Further dye tracking experiments confirm that diurnal forcing strengthened the northwestward longshore freshwater transport (NLFT) of the Yangtze River by $5.2 \times 10^9 \text{ m}^3$ and reduced the mean water age of 7 days. Sensitivity experiments using different forcing combinations suggest that the diurnal wind, that is, the land–sea breeze, is the key to developing the dipole pattern of salinity change and the NLFT. Through the experiment, the land–sea breeze induced a mean clockwise circulation offshore of the Yangtze River estuary. The above changes resulted from both the nonlinearity of wind stress averaging (i.e., the square nature of wind stress) and the baroclinic adjustment related to the diurnal salinity variation, which is directly connected to the diurnal swing of the Yangtze River front. The baroclinic adjustment generated a dipole pattern of vorticity changes offshore of the Yangtze River estuary and a coherent northwestward jet current strengthening the NLFT. These processes developed the summer dipole pattern of the salinity change.

1. Introduction

Because of the diurnal forcing of solar insolation, atmospheric states within the boundary layer, such as the land–sea breeze, feature a strong diurnal cycle. The influence of diurnal forcing also extends to the ocean, affecting the upper-ocean temperature (Sverdrup et al. 1942). The daytime warming generates a “thermodynamic diurnal stratified layer” (Fairall et al. 1996a) and increases the sea surface temperature (SST). The nocturnal mixing deepens the mixed layer (Bernie et al. 2005) and thus reduces SST (Price et al. 1986). Through the nonlinear oceanic adjustment process, the diurnal SST relates to the seasonal and intraseasonal SST

variabilities, which are called the “diurnal effects” in some studies.

Recently, the impacts of diurnal forcing on sea surface salinity (SSS) have drawn considerable attention. The diurnal cycle of salinity may influence upper ocean stratification (Lukas and Lindstrom 1991; Montégut et al. 2007), which in turn affects SST and air–sea fluxes of heat and momentum (Soloviev and Lukas 2006; Anderson et al. 1996). Although the diurnal SSS variability is small (Cronin and McPhaden 1999), it is appreciable by the adequate in situ instrumentation (Cronin and McPhaden 1999; Drushka et al. 2014) and satellite remote sensing (Fine et al. 2015). Without considering the events of extreme rainfalls, the diurnal SSS variation over the tropical ocean is mainly caused by the asymmetric evaporation and mixing during the day and night (Hodges

Corresponding author: Huiwang Gao, hwgao@ouc.edu.cn

DOI: 10.1175/JPO-D-19-0200.1

© 2020 American Meteorological Society. For information regarding reuse of this content and general copyright information, consult the [AMS Copyright Policy \(www.ametsoc.org/PUBSReuseLicenses\)](https://www.ametsoc.org/PUBSReuseLicenses).

and Fratantoni 2014; Fine et al. 2015). The diurnal warming increases SST during the day, thus resulting in strong diurnal evaporation, leading to a saltier, warmer, and more stable surface layer. At night, the surface cooling induces mixing so that the vertical entrainment decreases the SSS.

Further studies also suggest that the diurnal SSS can be driven by horizontal transport induced by the diurnal forcing, especially in the area near river estuaries. Shipboard observations for the Maipo River plume (Piñones et al. 2005) and Neuse River plume (Reynolds-Fleming and Luettich 2004) suggest that the sea breeze (wind blowing from the ocean toward the land due to the air pressure differences created by the different heat capacities of water and land) weakens the expansion of diluted water while the land breeze (wind blowing from the land to the ocean) plays an opposite role. The diurnal current caused by the land–sea breeze can account for 15%–50% of the kinetic energy in surface currents over the Hudson River plume region (Hunter et al. 2007) that tune up the river plume variability and change the SSS (Hunter et al. 2010). Besides, the land–sea breeze can lead to an increase of local dissipation by propagating Poincaré waves away from the coast at the critical latitude (30°N or 30°S) and provides significant vertical mixing over the Mississippi River plume region, which may have a potential contribution to SSS (Zhang et al. 2010). The actual mechanism for diurnal forcing to drive SSS variation and its “salinity diurnal effects” remains elusive.

Very few studies have considered the impacts of diurnal forcing on a longer time scale (e.g., seasonal or longer) of salinity change, compared to the studies of SST response (Thushara and Vinayachandran 2014; Bernie et al. 2007; Drushka et al. 2014; Fine et al. 2015). Hunter et al. (2010) demonstrates that the land–sea breeze modulates the wind kinetic energy input, thus increasing the net freshwater transport along the Long Island coast and reducing the freshwater supplied to the New Jersey coastal current, which significantly changes the SSS. Using an idealized study, Qu and Hetland (2019) suggested that the simulation error of the river plume (the SSS change under different wind frequency) is proportional to the fraction of high-frequency wind energy missing. They concluded that 3- or 4-hourly winds were needed to properly capture the river plume variability (Qu and Hetland 2019). However, both Hunter et al. (2010) and Qu and Hetland (2019) only focused on the direct wind energy input to the ocean without considering the mechanisms associated with the current response.

The Yangtze River (also called Changjiang River), the sixth-largest river by discharge volume in the world (Wohl 2008; Vorosmarty et al. 1998), accounts for 90% of the total river discharge into the East China Sea

(ECS) (Shen et al. 1998; Chang and Isobe 2003). Since it is controlled by runoff and East Asian summer monsoon, the Yangtze River plume expands northeastward toward the Cheju Island in summer (Mao et al. 1963; Beardsley et al. 1985; Chang and Isobe 2003; Moon et al. 2009; Zhu et al. 1997). The summer extension of the Yangtze River plume substantially modifies the physical properties of the water mass such as salinity and stratification over the ECS (Wu et al. 2018). Furthermore, the Yangtze River plume may induce stratification that can lead to a current change (Kako et al. 2016). The Yangtze River plume pattern is sensible to the high-frequency oceanic diurnal variability such as diurnal and sub-diurnal tides. Tidal mixing leads to a detachment of the Yangtze River plume (Lie et al. 2003; Moon et al. 2010; Shi and Lu 2011; Wu et al. 2011; Rong and Li 2012). The Stokes drift induced by tidal motion forms a residual current, which transports Yangtze River freshwater northwestward along the Jiangsu Coast in the summer (Wu et al. 2014). However, very few studies have focused on the Yangtze River plume response to the diurnal atmospheric forcing. A preliminary study over the ECS by Yu et al. (2017) suggested that the diurnal forcing is likely to affect the Yangtze River diluted water and its front and thus has the potential to change temperature. In this study, we explore the impacts of diurnal forcing on the summer salinity changes in the ECS and investigate the mechanisms that control salinity changes. This can enhance our understanding of modeling long-term material transport, such as marine debris and oil spill disasters, in the midlatitude shelf sea.

The structure of this paper is as follows. Section 2 describes the methodology and numerical experiments. Section 3 presents the results of the model experiments, and section 4 explains the formation mechanism for the salinity deviation patterns induced by the diurnal forcing. Section 5 examines the sensitivity of the salinity deviation patterns to the forcing frequency. Conclusions and suggestions are provided in section 6.

2. Methodology and numerical experimental design

a. Ocean model configuration

In this study, a moderate-resolution Regional Ocean Modeling System (ROMS) model (Shchepetkin and McWilliams 2005) is applied to investigate the summer salinity change induced by the diurnal atmospheric forcing in the ECS. The model has been shown to simulate diurnal and seasonal temperature variations (see Fig. 3 in Yu et al. 2017). The model configuration used here is the same as that used in Yu et al. (2017), including the Mellor–Yamada level-2.5 turbulence closure scheme

(Mellor and Yamada 1982) for vertical mixing and the Smagorinsky diffusion parameterization (Smagorinsky 1963) for horizontal diffusions. The model resolution is $1/18^\circ$ (~ 6 km) and ranges from 24° to 41.3°N and from 117° to 132°E (Fig. 1). The model has 30 terrain-following “S” levels in the vertical direction with higher resolutions near the sea surface using the Shchepetkin’s double stretching function (Shchepetkin and McWilliams 2009), and the thickness of the top model layer is less than 1 m (Bernie et al. 2005). We integrate the model for 5 years from 1 January 2011 to 31 December 2015, and hourly model outputs are stored for analysis.

Before running a 5-yr simulation, the model is spun up for 30 years, from 1 January 1981 to 31 December 2010, starting from the climatological temperature, salinity and flow fields. The Simple Ocean Data Assimilation Version 3 (SODA3) reanalysis data with a spatial resolution of $1/4^\circ$ (~ 27 km) and a temporal resolution of 5 days (Carton et al. 2018) is used to create the low-frequency lateral boundary conditions of sea surface height (SSH), currents, temperature and salinity. Ten principal tidal constituents— M_2 , S_2 , N_2 , K_2 , K_1 , O_1 , P_1 , Q_1 , M_f , and M_m —derived from the Oregon State University global inverse tidal model of TPXO7.0 (Egbert et al. 1994; Egbert and Erofeeva 2002), are specified as the high-frequency lateral boundary conditions.

b. Atmospheric forcing and numerical experiments

Atmospheric forcing is critical to temperature and salinity responses from the diurnal to seasonal time scales, and is therefore described first. Solar insolation was directly employed using a double exponential absorption function (Paulson and Simpson 1977) with Jerlov water type II parameters [light absorption parameters for dirty coastal water; see Table 2 in Paulson and Simpson (1977)]. The radiative cooling caused by long wave radiation was calculated by the Berliand algorithm, based on the blackbody radiation formula (Berliand 1952). The latent heat, sensible heat, and wind stress were calculated by the COARE 3.0 bulk formulas (Fairall et al. 1996b; Fairall et al. 2003). The “cool skin” effects on sea surface heat and vapor fluxes were also considered using an empirical correction scheme (Fairall et al. 1996a).

The 6-hourly National Centers for Environmental Prediction–National Center for Atmospheric Research (NCEP–NCAR) reanalysis data (Kalnay et al. 1996) are used to provide atmospheric forcing for the model spinup run, including wind speed (10 m), solar radiation, air temperature (2 m), air pressure (2 m), precipitation rate, cloud fraction, and relative humidity. However, for the 5-yr sensitivity experiments, the surface winds and solar radiation, which control the oceanic diurnal cycle in

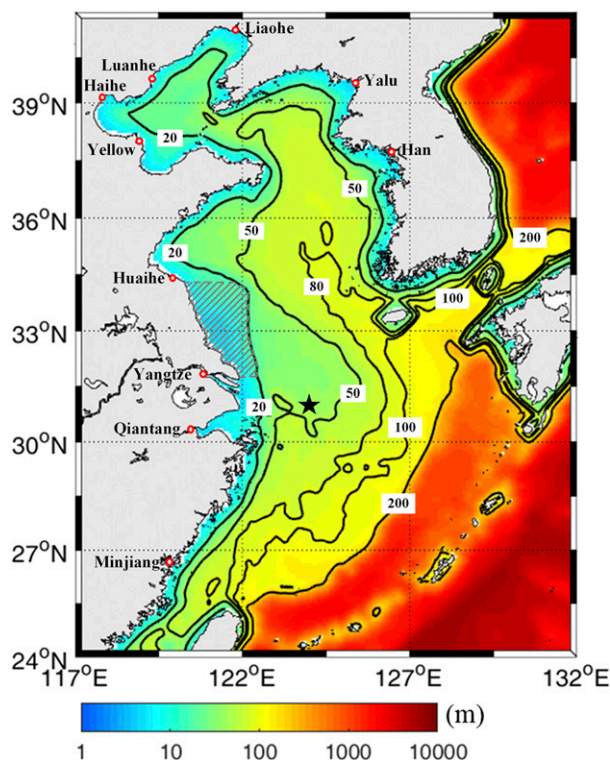


FIG. 1. Model domain and bottom topography. Contour lines indicate water depth (m). Red circles show river estuary locations. The hatches along Jiangsu Coast mark the region selected to calculate the northwestward transport of Yangtze River freshwater. The black pentagram is the buoy site used in the study.

the ECS (see Table 2 in Yu et al. 2017), are replaced by the fifth generation of the European Centre for Medium-Range Weather Forecasts (ECMWF) atmospheric reanalysis of the global climate (ERA5) dataset (Copernicus Climate Change Service 2017). This reanalysis is a state-of-the-art atmospheric reanalysis product, which provides hourly estimates of the meteorological parameters with a $1/4^\circ$ resolution. The hourly output data allow us to conduct sensitivity experiments with different time resolutions. Because the model resolution ($1/18^\circ$) is much higher than the reanalysis data, atmospheric forcing was linearly interpolated to each model point for every time step. Table 1 shows four sensitivity experiments in combinations of daily mean and hourly diurnal data of sea surface wind and solar radiation obtained from the ERA5 dataset. Other atmospheric forcing variables used daily mean values, averaged from the 6-hourly NCEP–NCAR data in the four sensitivity experiments.

c. River discharge

Freshwater input from rivers, especially the Yangtze River, is another key factor contributing to the SSS distribution in summer (Kim et al. 2009; Moon et al.

TABLE 1. List of model experiments conducted in this study. The daily 10-m wind is obtained by averaging hourly 10-m winds within a day. The same procedure is applied to daily solar heating.

	Forcing type
Daily case	Daily 10-m wind; daily solar heating
Diurnal case	Hourly 10-m wind; hourly solar heating
Case 1	Hourly 10-m wind; daily solar heating
Case 2	Daily 10-m wind; hourly solar heating

2009). The model had ten rivers inside the model domain, for example, the Yangtze, Yellow, Huaihe, Liaohe, Haihe, Luanhe, Minjiang, Qiantang, Yalu, and Han Rivers (river estuaries are shown in Fig. 1). Because the observed river runoff shows significantly interannual variability (Senju et al. 2006; also see Fig. 2) and the Yangtze River can account for 90% of the total river discharge into the ECS (Shen et al. 1998; Chang and Isobe 2003), monthly river discharge data from January 2011 to December 2015 at the Datong Station (Ministry of Water Resources 2011, 2012, 2013, 2014, 2015) are used in this study to account for the Yangtze River discharge (Fig. 2). Climatological monthly mean discharge data (not shown), derived from the Global River Discharge Project (<http://daac.ornl.gov/RIVDIS/rivdis.shtml>) (Vorosmarty et al. 1998) are used for other rivers. In the model, the river diluted water was discharged into all model layers (30 layers) at the upstream region of the river with 0 psu. The river temperature was derived from the climatological monthly SODA3 data at the nearest grid point because no observational data are available. We note that the river freshwater usually includes meltwater, which normally occurs in the early spring. This implies that the modeled river temperatures might be higher than the real values if the meltwater effect is ignored, such as in this study.

3. Model results

a. Summertime salinity in the ECS

The modeled summertime salinity in the ECS is initially verified by a comparison with field observational data, obtained from a summer cruise that was conducted by Ocean University of China from 5 to 25 July 2011. The detailed information for this summer cruise can be found in Quan et al. (2013).

Compared to observations (Fig. 3a), the spatial distribution of salinity at the 5-m depth is reasonably reproduced by both the diurnal case (the hourly forcing case; Fig. 3b) and daily case (the daily forcing case; Fig. 3c). The salinity distribution clearly shows a freshwater plume pattern with the salinity less than 32 psu, which extends northeastward from the Yangtze

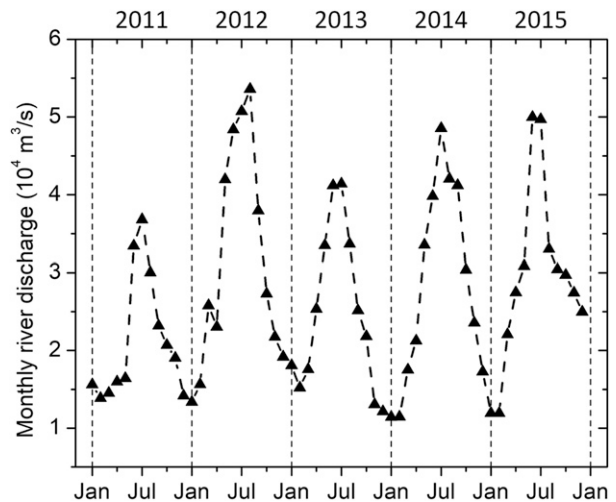


FIG. 2. The discharge rate of the Yangtze River for each month from 2011 to 2015.

River estuary to the Cheju island. These results are consistent with the previous studies (Mao et al. 1963; Beardsley et al. 1985; Su and Weng 1994; Chang and Isobe 2003; Moon et al. 2009; Zhu et al. 1997). However, a large difference (about 12 psu) exists between the simulated and observed salinities in the vicinity of the Yangtze River estuary (e.g., the location with the lowest salinity in Fig. 3a). This is possibly caused by model errors and the nominal 6-km resolution river mouth topography used in the model that cannot capture the detailed salinity change in the river/ocean interaction. However, the model can still reasonably simulate the summertime salinity in the ECS. The root-mean-square error (RMSE) is 2.84 psu in the diurnal case, slightly better than that in the daily case (2.98 psu). The relative salinity biases, defined as the ratio of the model salinity bias to the observed salinity [i.e., $(S_{\text{model}} - S_{\text{obs}})/S_{\text{obs}}$, where S_{model} and S_{obs} are simulated and observed salinities, respectively], in both the diurnal and daily cases are between -20% and 20% in more than 90% of the hydrological stations (Fig. 3d).

b. Time variation of salinity at the outer zone of the Yangtze River estuary

We further verify modeled SST and SSS in the ECS by comparing results with observations at a buoy site (124°E , 31°N) outside of the Yangtze River estuary from 1 May to 31 October 2015. This buoy was operated by Xiamen University and provided hourly SST and SSS (Figs. 4a,b). Unfortunately, due to the malfunction of the salinity sensor, no salinity observations are available from 11 July to 23 September (Fig. 4b) when the model river freshwater front passes this site from the diurnal case (Figs. 4c-e). Nevertheless, the rest of SSS observations still

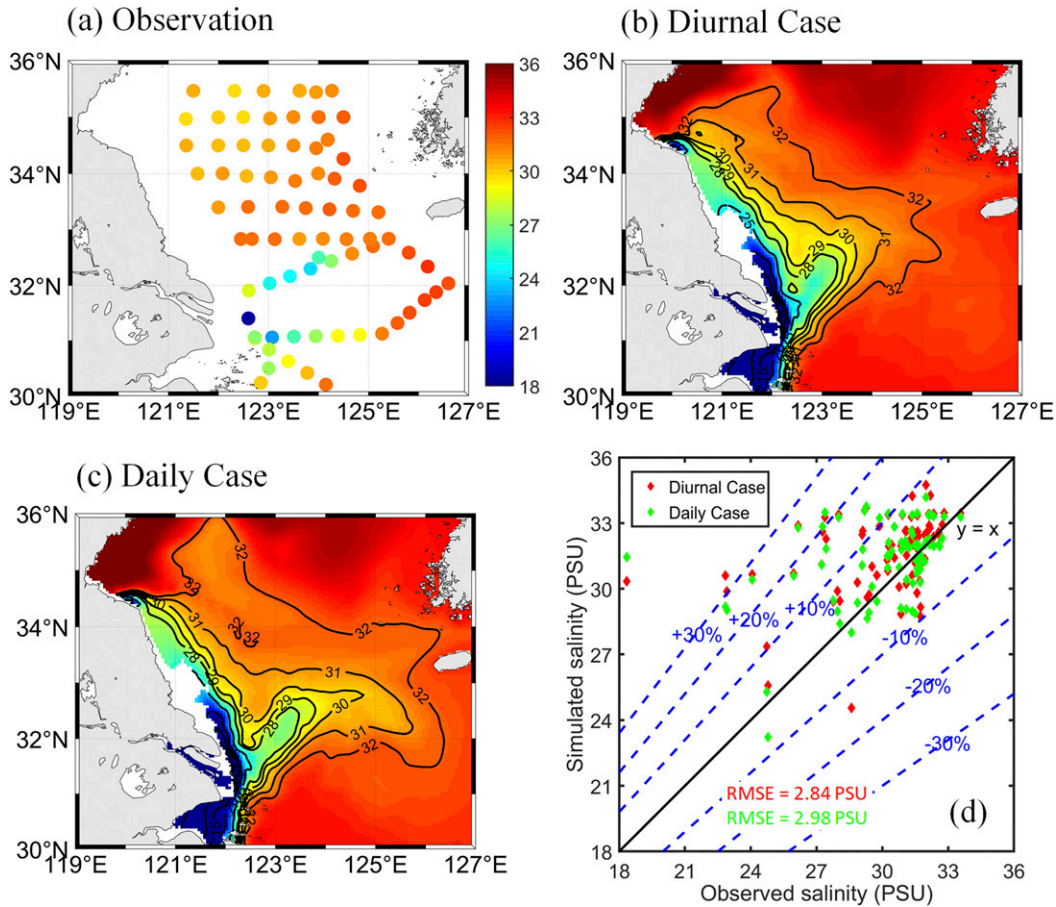


FIG. 3. Distributions of salinity at 5-m depth from the (a) summer cruise, (b) diurnal case, and (c) daily case. (d) Scatterplot diagram for model errors. Blue dashed lines in (d) represent the relative salinity deviation. Model salinities in (b) and (c) are time-averaged values over the duration of the summer cruise. However, model snapshot values corresponding to the exact times of the observational data are used in (d).

provide a great opportunity to verify the model performance. To highlight the impacts of diurnal atmospheric forcing on SST and SSS changes, the tidal signals in both the SST and SSS time series are removed (Figs. 4a,b) using the T-tide toolbox (Pawlowicz et al. 2002).

Similar to the temperature response reported by Yu et al. (2017), the diurnal forcing decreases the systematic bias of SST about 0.5°C (Fig. 4a) due to its direct modulation of surface heat fluxes and vertical mixing (Yu et al. 2017). Regarding to the SSS, a RMSE difference of 0.24 psu is found between the diurnal case and the daily case but the diurnal forcing does not improve the salinity simulation at this station, that is, larger RMSE for SSS in the diurnal case than in the daily case (Fig. 4b). One possible reason is the 2° NCEP–NCAR daily precipitation data used in both simulations does not capture the intensity of a heavy precipitation event near this site from 11 to 12 May (figures not shown), causing the model’s SSS bias from negative (before 11 May) to

positive (after 12 May). This is evidenced by a much larger SSS drop in the observation than in both diurnal and daily cases during that day (Fig. 4b).

Nevertheless, the model reasonably simulates the diurnal SST and SSS variations at this buoy site. During the observational period from May to October, the average diurnal amplitude changes (daily maximum minus daily minimum) of SST and SSS from the diurnal case are 0.22°C (red line in Fig. 5a) and 0.06 psu (red line in Fig. 5b), respectively, while those from observations are 0.23°C for SST (black line in Fig. 5a) and 0.07 psu for SSS (black line in Fig. 5b). The correlation of diurnal SST between the diurnal case and buoy observation is 0.94 ($P < 0.01$; Fig. 5a) and that of diurnal SSS is 0.62 ($P < 0.01$; Fig. 5b).

c. Dipole-pattern salinity deviation induced by diurnal forcing in summertime

While the model simulations from both the diurnal case and the daily case for salinity in the ECS are comparable

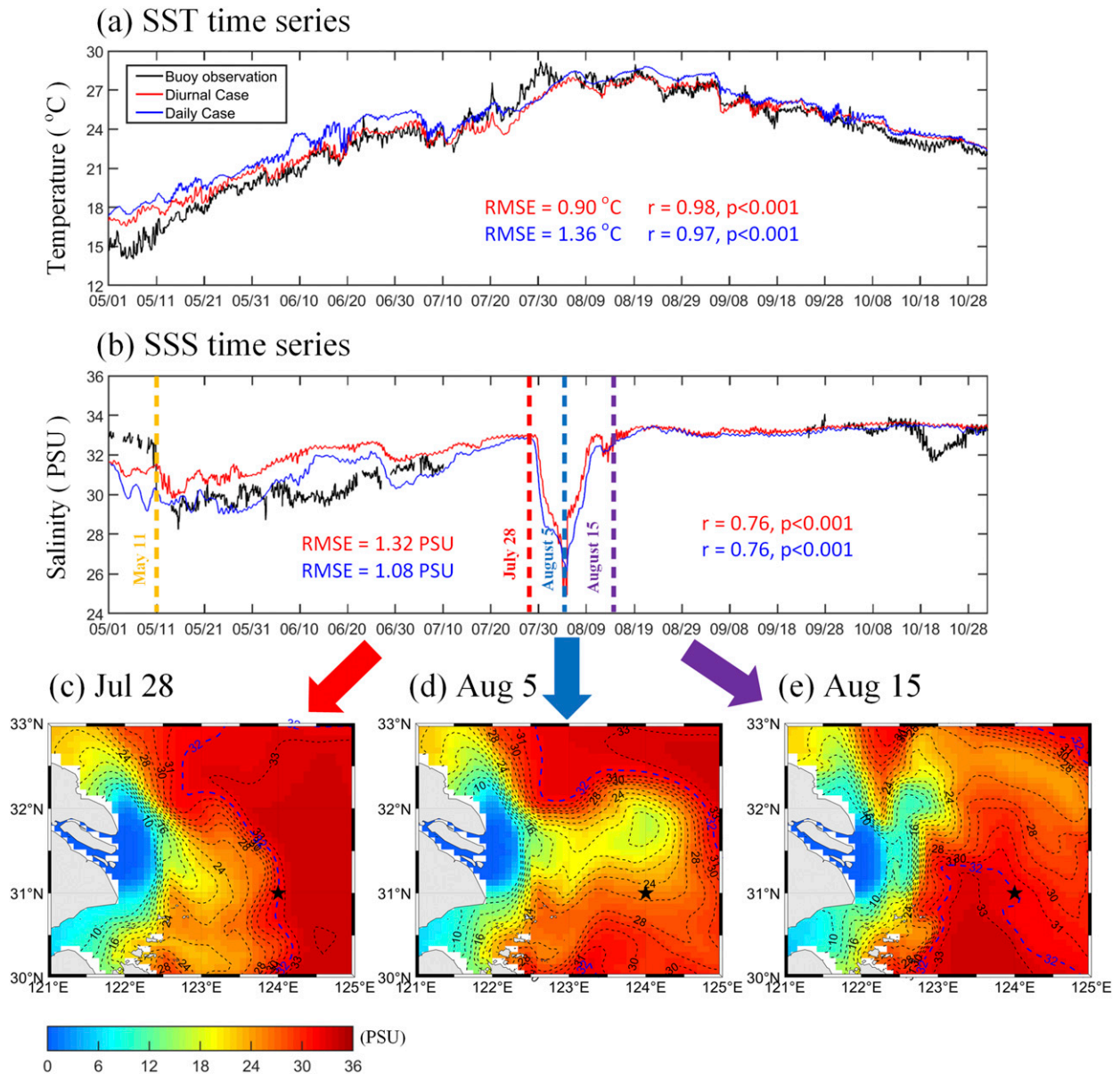


FIG. 4. Time series of detided hourly (a) SST and (b) SSS from 1 May to 31 Oct 2015 for the diurnal case (red curve), the daily case (blue curve), and observations (black curve) at the buoy site (31°N , 124°E). The spatial distribution of daily mean SSS on (c) 28 Jul, (d) 5 Aug, and (e) 15 Aug 2015 in the diurnal case. Buoy temperature and salinity are measured at the depth of 0.5 m, and thus the model SST and SSS are linearly interpolated to this depth. Contour lines in (c)–(e) represent the salinity field and the black pentagram is the buoy site.

(Figs. 3 and 4), the discrepancies between these two numerical experiments do exist, indicating that the diurnal forcing may regulate the salinity distribution in summer. The diluted water, by the extension of the Yangtze River freshwater, is commonly identified by the 32-psu isohaline (Kako et al. 2016; Su and Weng 1994). This 32-psu isohaline only reached the southwest of Cheju Island in the diurnal case (Fig. 3b) but almost surrounded Cheju Island in the daily case (Fig. 3c). This implies that the

Yangtze River plume can expand more northeastward in the daily case than in the diurnal case (Fig. 3b versus Fig. 3c).

To understand this summertime salinity variation induced by the diurnal forcing in detail, we present the monthly SSS difference between the diurnal case and the daily case from May to August 2011 in Fig. 6. A dipole-pattern SSS difference is clearly shown in the ECS; a positive 1–2-psu salinity difference (i.e., diurnal

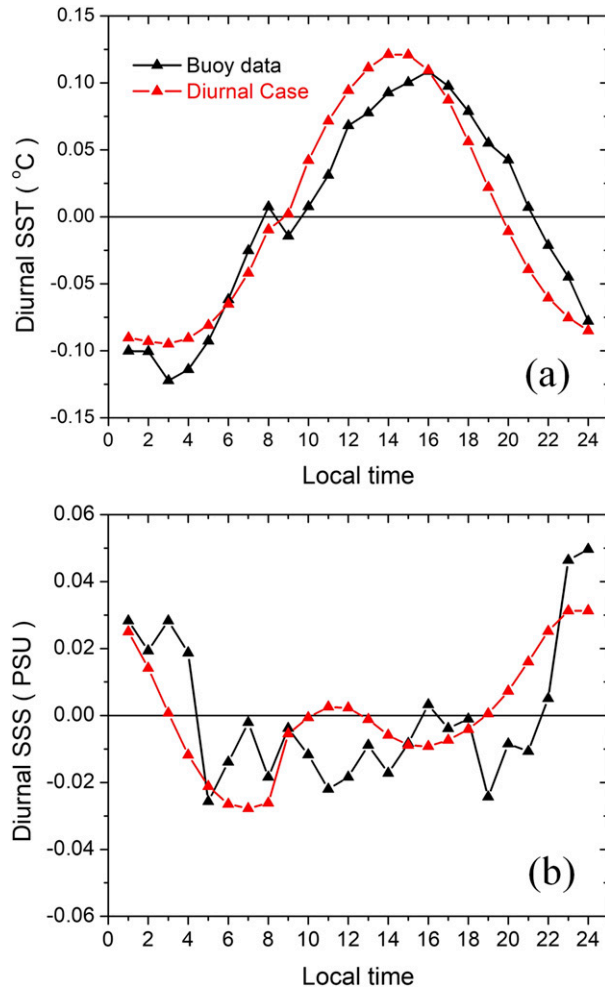


FIG. 5. Diurnal variations (hourly data minus their daily mean) of (a) SST and (b) SSS at the buoy site. Data are averaged during the observation period from May to October 2015. The black line denotes the buoy observation, and the red line is the diurnal case.

forcing increases the SSS) outside the Yangtze River estuary and a negative difference from -1 to -0.5 psu (i.e., diurnal forcing decreases the SSS) in Jiangsu Coast. The range of this dipole pattern evolved over time. The positive SSS difference was extended northeastward (shading color in Figs. 6a–c) to the vicinity of Cheju Island, from May to July, when the Yangtze River dilute water expanded northwestward (gray dashed lines in Figs. 6a–c). Consequently, its magnitude gradually decreased from July to August as the freshwater expansion slowed down (Figs. 6c,d). The negative SSS difference region continuously expanded northwest along the Jiangsu Coast from May to August (Figs. 6a–d). Apparently, this dipole-pattern of salinity difference was induced by the diurnal forcing, which was the only difference between these two numerical experiments.

We further examined the causes in the following sections.

d. Quantification of freshwater transport

To quantify the impacts of diurnal forcing on the Yangtze River freshwater transport, a few experiments with dye tracer tracking were conducted, using the passive tracer-tracking model in ROMS. In the passive tracer-tracking model, the dye tracer, which is treated as a scalar in a model, does not interact with any model variable and is only transported by advection and diffusion. Dye tracers are released from the Yangtze River estuary with a concentration of 100, which can represent the Yangtze River freshwater proportion. In the dye tracking experiments, the water age of Yangtze River freshwater is calculated based on the constituent-oriented age and residence time (CART) theory (Deleersnijder et al. 2001; Delhez et al. 1999). The water age is defined as the elapsed time since the water mass leaves the place where the passive dye tracer is released. It is a useful measure of the time scale for general matter transport and has been successfully applied to many coastal studies, especially for Yangtze River freshwater water transport (Zhu and Wu 2018; Wang et al. 2015).

In the passive tracer-tracking model, the dye tracer concentration and water age are calculated using the following equations:

$$\frac{\partial C}{\partial t} + \nabla \cdot (\mathbf{V}C - \mathbf{K} \cdot \nabla C) = 0, \tag{1}$$

$$\frac{\partial \alpha}{\partial t} + \nabla \cdot (\mathbf{V}\alpha - \mathbf{K} \cdot \nabla \alpha) = C, \tag{2}$$

$$a = \frac{\alpha}{C}, \tag{3}$$

where C is the dye concentration, \mathbf{V} the velocity vector, \mathbf{K} the diffusivity tensor, α the age concentration, and a the water age (the average elapsed time since the dye tracer released).

The distributions of dye concentration (Figs. 7a,b) and water age (Figs. 7d,e), in both the diurnal case and daily case, clearly show a plume pattern that originated from the Yangtze River diluted water. Due to mixing and dilution processes, the dye concentration decreases with the increasing distance away from the river mouth (Figs. 7a,b). The simulated water age in the Jiangsu Coast ranges from 80 to 160 days, with an average of 120 days, and this result is consistent with a previous study (Zhu and Wu 2018). A dipole pattern is also found in the dye concentration difference between the diurnal case and the daily case (Fig. 7c). The negative dye concentration deviation (from -6 to -1) outside

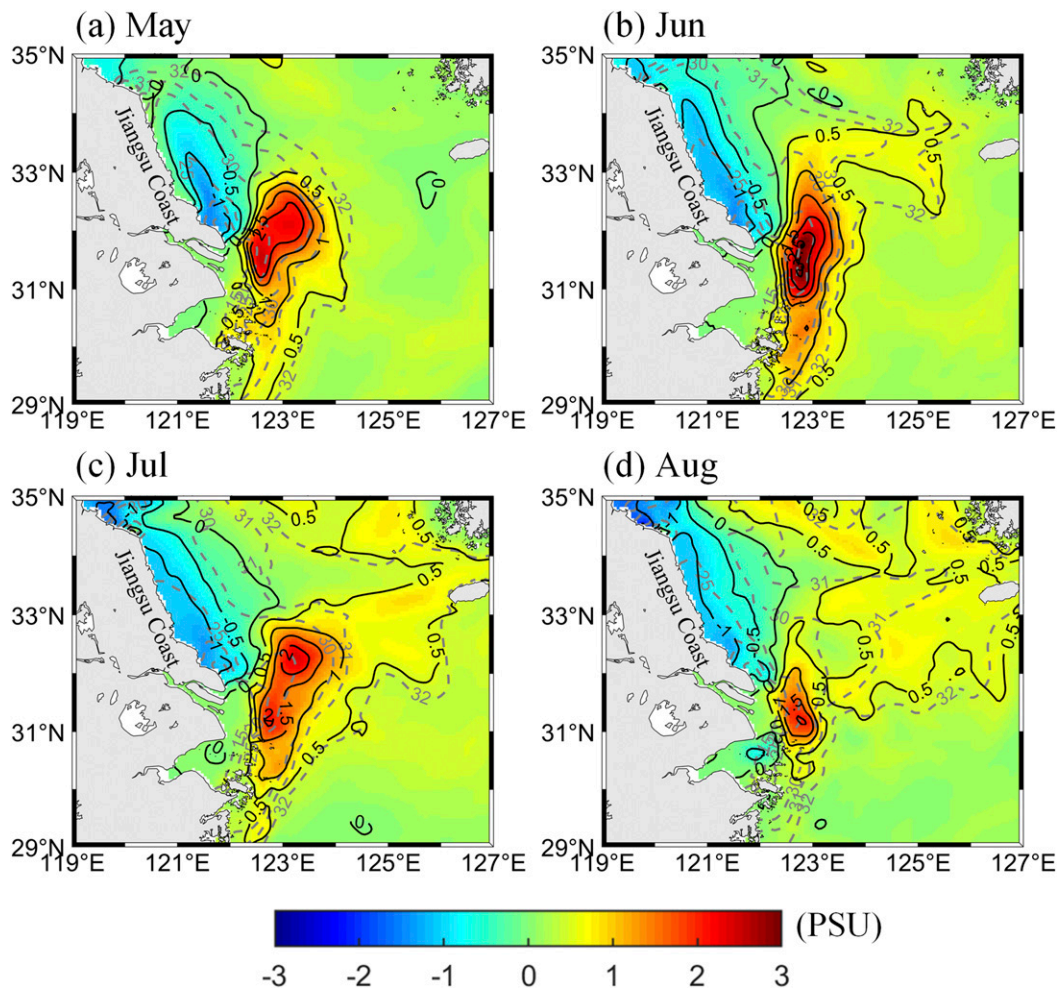


FIG. 6. Monthly mean differences of SSS between the diurnal case and the daily case in (a) May, (b) June, (c) July, and (d) August 2011. Gray dashed lines show monthly SSS in the daily case.

of the Yangtze River estuary and the positive deviation (1–3) in Jiangsu Coast echoes our early discussion that the diurnal forcing enhanced more Yangtze River freshwater transport northwestward along Jiangsu Coast rather than heading northeastward. The water age difference between these two experiments also suggests this change; positive water age deviation of 5–10 days in the northeast region of the Yangtze River plume and negative deviation from –10 to –5 days in Jiangsu Coast (Fig. 7f). The shorter water age near the Jiangsu Coast suggests that it took less time to transport the Yangtze River freshwater northwestward along Jiangsu Coast in the diurnal case than in the daily case.

To quantify this enhanced freshwater transport, we calculated the changes of the volume and freshwater age of NLFT in the selected region, shown as the hatch area in Fig. 7f. Using the dye concentration, which

also represents freshwater proportion in water mass, the freshwater volume and freshwater age of NLFT can be estimated using the following equations:

$$FV = \left\langle \int \frac{C}{C_{\text{Ini}}} dv \right\rangle, \quad (4)$$

$$FA = \frac{1}{V} \left\langle \int a dv \right\rangle, \quad (5)$$

where FV and FA are the freshwater volume and age, respectively, C the passive tracer concentration, C_{Ini} the initial tracer concentration when the tracer is released and is set to 100 in this study, a the water age calculated from Eq. (3), $\langle \cdot \rangle$ the time average operator, V the total water volume in the selected region, and dv the differential volume.

The average volume of the NLFT in the selected region from May to August during the 5-yr-period (from

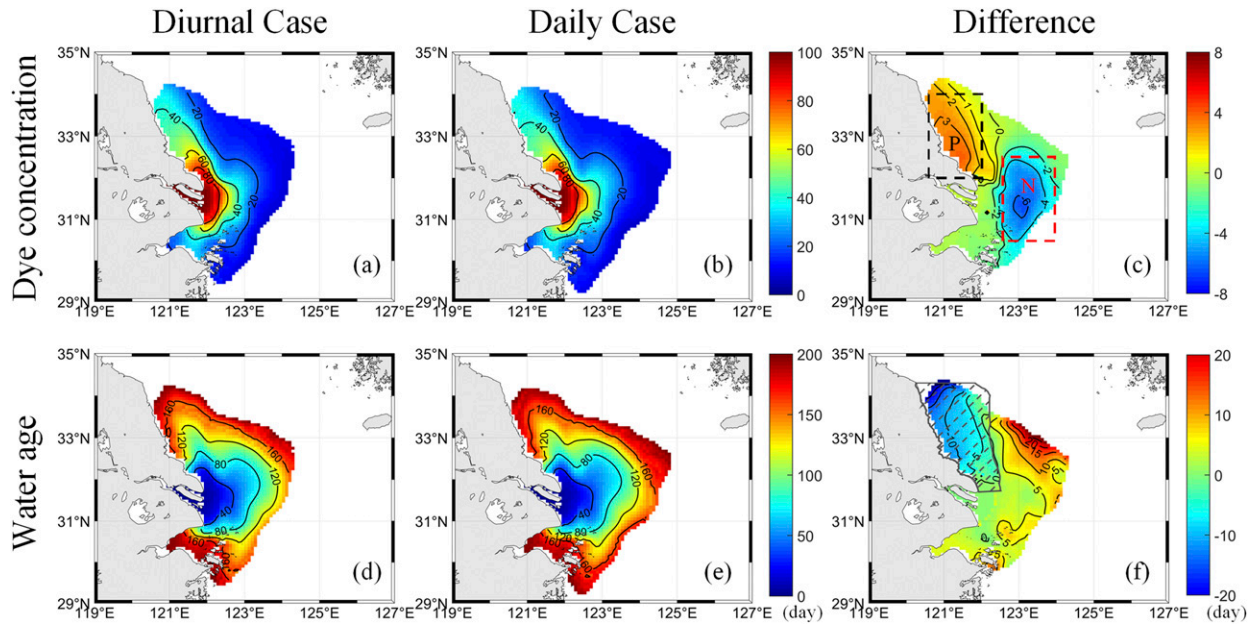


FIG. 7. Distributions of (top) dye tracer concentration and (bottom) water age of Yangtze River diluted water in (a),(d) the diurnal case, (b),(e) the daily case and (c),(f) the difference between the diurnal case and the daily case. Values for this figure are averaged over May–August from 5 years of simulation. Results in the region where water age was above 200 days were not shown to avoid excessive values of water age in (d) and (e). The areas surrounded by black and red dashed lines are selected regions used to calculate salinity deviations in Fig. 8 and Table 2. The hatching in (f) is the selected region for the NLFT calculation.

2011 to 2015) sensitivity experiments was 10.40×10^{10} and $9.88 \times 10^{10} \text{ m}^3$ in the diurnal case and the daily case (Table 2), respectively. Compared to the daily case, the volume of NLFT was increased by $0.52 \times 10^{10} \text{ m}^3$ (~5%) and the freshwater age of NLFT was decreased by 7 days (~4%) (Table 2) in the diurnal case. These changes in the volume and freshwater age of NLFT in the diurnal case correspond to the reduced SSS in the P region (by 0.9 psu, ~4%) and the increased SSS in the N region (by 1.7 psu, ~7%) (Table 2; see Fig. 7c for the P and N regions). The volume difference of NLFT correlates very well with the salinity deviation in the P region (negative correlation $r = -0.98, p < 0.01$) and correlates moderately with the salinity deviation in the N region (positive correlation $r = 0.69, p < 0.2$) over the 5-yr-period model integration (Fig. 8).

4. Mechanisms study

a. Key diurnal factor contributing to salinity changes

To further clarify the mechanism involved in the salinity changes, we first carried out two sensitivity experiments (Table 1) to address the key factor in the diurnal forcing. Either the wind (case 1) or solar insolation (case 2) is changed from daily to hourly while the rest of the configurations is kept the same as those in the daily case. Compared to the daily case, the case

1 shows very similar salinity result to that of the diurnal case; decreased and increased SSS by 0.9 and 1.6 psu over regions P and N, respectively. This is associated with increased mean volume of NLFT ($5.3 \times 10^9 \text{ m}^3$) and decreased freshwater age by 8 days (Table 2). On the other hand, the case 2 shows almost no difference in salinity compared to the daily case (Table 2). These results suggest that the diurnal wind effect alone (case 1) can sufficiently explain the dipole pattern of the salinity difference and the changes in NLFT in the diurnal case, while the direct heating induced by the diurnal insolation (case 2) plays no role on the salinity changes.

TABLE 2. Average sea surface salinity in the P and N regions (see Fig. 7c) from May to August during the 5-yr-period model integration and the volume and freshwater age of northwestward longshore freshwater transport (NLFT) of diluted Yangtze River water in different experiments.

	Salinity in region P (psu)	Salinity in region N (psu)	NLFT	
			Mean volume ($\times 10^{10} \text{ m}^3$)	Water age (day)
Daily case	20.3	24.0	9.88	166
Diurnal case	19.4	25.7	10.40	159
Case 1	19.4	25.6	10.41	158
Case 2	20.3	24.0	9.87	166

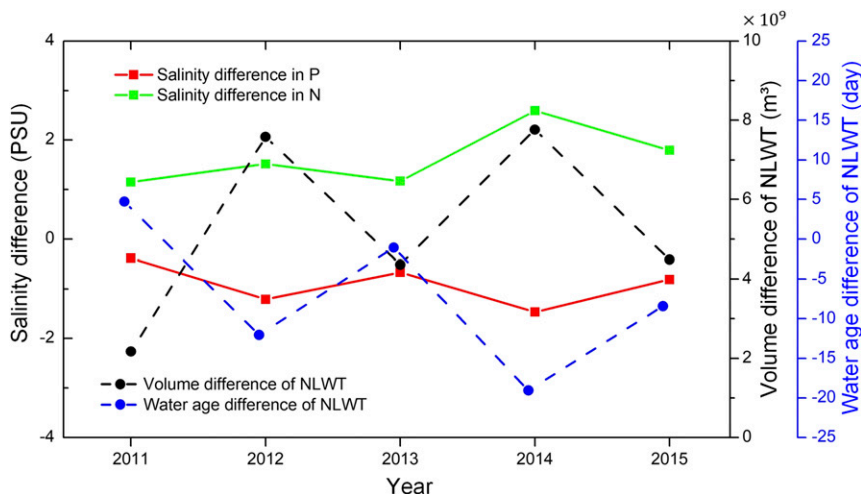


FIG. 8. Volume (black dashed line) and freshwater age (blue dashed line) differences of Yangtze River NLFT in selected region shown in Fig. 1 and the SSS differences in the P (red line) and N (green line) regions between the diurnal case and the daily case. The P and N regions are shown in Fig. 7. Values for this figure are averaged from May to August of each year.

b. Salinity budget and clockwise circulation anomaly

The above sensitivity experiments suggest that the diurnal wind is the primary contributor to the summertime salinity change. To further explore how the diurnal wind generates the dipole pattern of the salinity difference in the ECS, we first evaluate the changes of the seasonal mean (from May to August over the 5-yr integration) salinity budget between the diurnal case and the daily case in the mixed layer. The mixed layer salinity budget can be expressed as follows (Kako et al. 2016):

$$\frac{\partial S_m}{\partial t} = -\mathbf{U}\nabla \cdot S_m + \frac{(E - P)S_m}{h_m} + \text{residual}, \quad (6)$$

where S_m is the mixed layer salinity, \mathbf{U} the horizontal current vector in the mixed layer, E and P the evaporation and precipitation at the sea surface, respectively, and h_m the mixed layer depth. The mixed layer depth in this study is defined as the minimum depth of the vertical density gradient greater than 0.01 kg m^{-1} (Thomson and Fine 2003). The term on the left-hand side of Eq. (6) is the local change rate (or tendency) of salinity in the mixed layer. The three items on the right-hand side of Eq. (6) are horizontal advection, surface salination forcing, and residual term, respectively. The residual term includes salinity diffusion and entrainment from the bottom of the mixed layer.

The difference of the salinity tendency between the diurnal case and the daily case shows a dipole pattern in summer (Fig. 9a), a positive change of $1\text{--}2 \times 10^{-6} \text{ psu s}^{-1}$ outside of the Yangtze River estuary and a negative

change from -5 to $-1 \times 10^{-6} \text{ psu s}^{-1}$ in the Jiangsu Coast. If we integrate this tendency difference for a period of one month (over 30 days), we obtain salinity changes on the order of 1 psu, consistent with the salinity changes presented in section 3. The dipole-like salinity tendency difference (Fig. 9a) was mainly caused by the horizontal advection (Fig. 9b) and the surface salination forcing (Fig. 9c). The residual term has only limited impact on this salinity tendency difference (Fig. 9d).

Interestingly, the signs of the horizontal advection (Fig. 9b) and surface salination forcing (Fig. 9c) are opposite and this implies a large compensation between these two terms. And as expected, this compensation mainly exists at the western side of the ocean domain (i.e., close to the coastal region), the reasons are twofold. As the surface salination forcing is modulated by the ratio of the salinity S_m to the local mixed layer depth h_m . Moving away from the coast, the faster deepening rate of the mixed layer depth (figure not shown) overpowers the slower salinity increasing rate and, as a result, quickly damps out the surface salination forcing toward the east (i.e., away from the coast). But toward the coastal region, where the mixed layer is shallower and the salinity change becomes important in the surface salination forcing (e.g., S_m increases) enhances negative salination forcing (e.g., a negative response as $E - P$ in Eq. (6) is negative; Figs. 9b,c) and vice versa, acting like a restoration force. While the horizontal advection and surface salination forcing had the same magnitude, the horizontal advection (Fig. 9b) had the same sign as the salinity tendency (Fig. 9a). This means that although

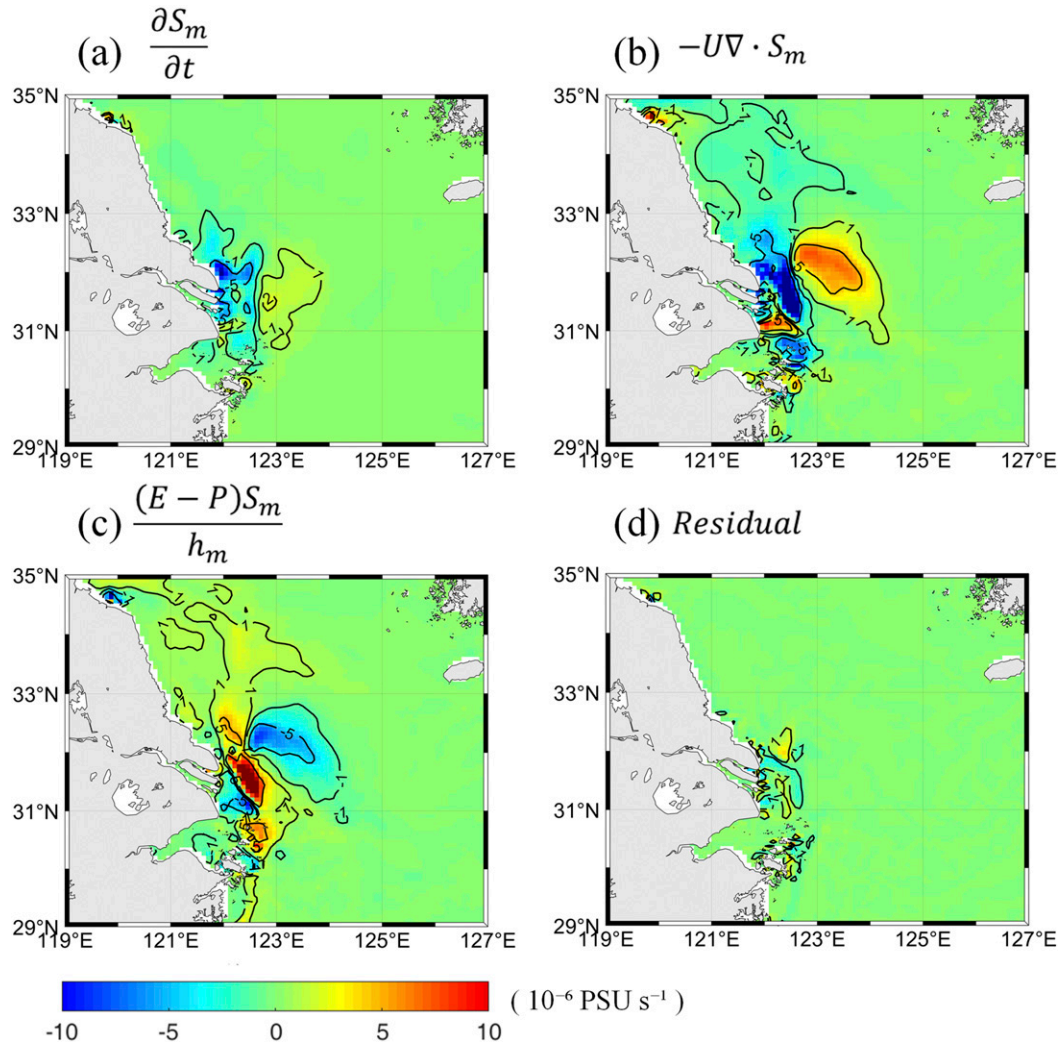


FIG. 9. Distribution of (a) salinity change rate, (b) horizontal advection, (c) surface salination forcing, and (d) the residual term differences between the diurnal case and the daily case in the mixed layer salinity budget.

there was strong competition between the advection and surface salination forcing (Figs. 9b,c), the changes caused by the advection term (Fig. 9b) still play a dominant role in forming the dipole pattern of the salinity difference between the diurnal and the daily case in this study.

The summer (average from May to August) SSS and the ocean surface flow for the diurnal case, the daily case, and their differences are further provided in Fig. 10. Both the diurnal case (Fig. 10a) and the daily case (Fig. 10b) show that the Yangtze River diluted water had two expansion branches in summer. One was the northeastward offshore freshwater transport path conducted by the East Asian summer monsoon (Mao et al. 1963; Beardsley et al. 1985; Chang and Isobe 2003; Moon et al. 2009; Zhu et al. 1997) and the other was the NLFT conducted by the residual currents

(Wu et al. 2014). The surface flow difference (Fig. 10c) further suggested a clockwise circulation difference, which was induced by the diurnal wind in the frontal region of Yangtze River plume in summer. As discussed above, the advection term dominates the salinity tendency changes between the diurnal case and the daily case. This clockwise frontal circulation anomaly (CFCA) results in a decrease in east-northeastward transport of Yangtze River freshwater and an increase in north-northwestward NLFT of Yangtze River freshwater (Fig. 10c).

c. Flow response to land–sea breeze

To better understand this CFCA, induced mainly by the diurnal wind, we further examine the summer (May–August) 10-m wind and surface flow differences (the diurnal case minus the daily case) over the Yangtze

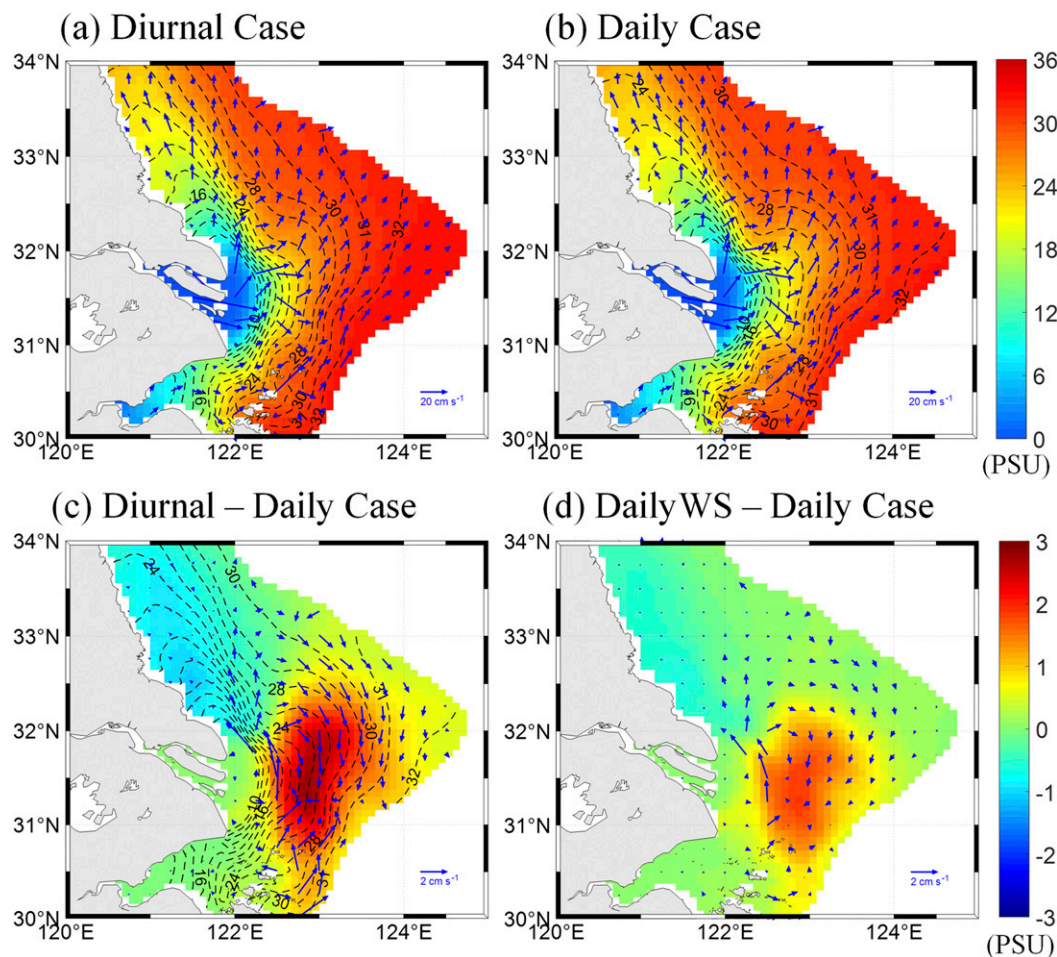


FIG. 10. Distribution of summertime (average from May to August over the 5-yr-period model simulation) SSS and surface flow field in (a) the diurnal case, (b) the daily case and (c) their differences. (d) SSS and surface flow differences between the dailyWS case and the daily case in section 4c. Contour lines and shaded colors indicate salinity, and the blue vectors represent the flow field.

River plume region, where the water age was less than 200 days in the dye tracking experiments (Figs. 7d,e). Figure 11a shows the time series of the hourly mean (averaged over the same hour during the 5-yr model integration) zonal wind (10-m U wind) difference between these two experiments. Since the coastline orients approximately north-southward, the U wind is representative to show the land-sea breeze feature. The land breeze reached a maximal offshore wind speed of 0.4 m s^{-1} at 0300 local time (LT) while the sea breeze was at 2000 LT with an onshore wind speed of 0.4 m s^{-1} (Fig. 11a). We noted that, although Fig. 11a suggests a land-sea breeze feature, the averaged wind speed in Fig. 11a is most likely much weaker than the diurnal U -wind variation of any day at any location (usually few meters per second). This small value was due to the change of the coastline orientation and the complex topography over the land (Lin et al. 2019;

Huang et al. 2016). Therefore, a long-term average over a large area (as Fig. 11) would underestimate the magnitude of the land-sea breeze variation.

There was also a subdiurnal wind variation between the diurnal case and the daily case (0600–0800 LT and 1800–2000 LT in Fig. 11a). To examine the influence of the subdiurnal wind signal on the dipole-pattern salinity deviation, an experiment with an idealized diurnal wind forcing was conducted. The idealized diurnal wind was created by superimposing sinusoidal diurnal wind onto the daily case wind at each point and the magnitude of the sinusoidal wind was similar to the diurnal wind magnitude change in the diurnal case. The difference of this idealized case and the daily case can almost reproduce the dipole pattern and magnitude of the SSS change (figure not shown) discussed above. This implies that the diurnal wind signal plays the primary role in the dipole-pattern salinity change in this study.

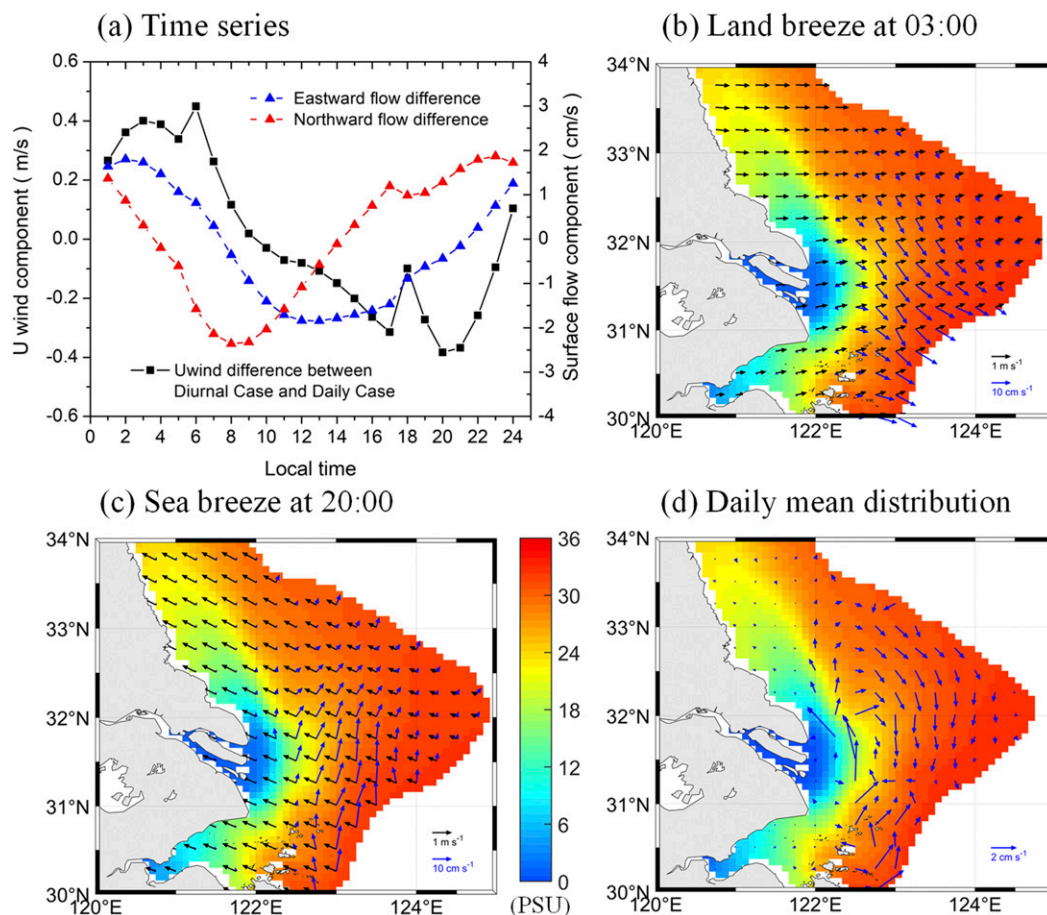


FIG. 11. (a) Time series of hourly mean 10-m U wind speed (black line), surface eastward flow (blue dashed line), and northward flow (red dashed line) differences between the diurnal case and the daily case in the Yangtze River plume region (where the water age was less than 200 days in dye tracking experiments) averaged from May to August over the 5-yr-period model integration; the distributions of SSS in the diurnal case (shading color), the 10-m wind (black vectors) and surface flow (blue vectors) differences between the diurnal case and the daily case at (b) the land breeze of 0300 LT and (c) the sea breeze of 2000 LT; and (d) the daily mean distributions of SSS (shading color) in the diurnal case and surface flow difference (blue vectors) between the diurnal case and the daily case.

The 10-m wind field presents a clockwise rotation due to land–sea breeze and the Coriolis effect, leading to a clockwise surface flow deflection response (Figs. 11b–d). The deflection angle of the surface ocean current direction from 10-m wind vector reached its maximum value of 90° at the sea breeze (Fig. 11c), when the surface wind direction aligns with the mean southeasterly monsoonal wind. The deflection angle can also be less than 20° in other times (figure not shown). Therefore, by integrating this diurnal ocean flow field, the asymmetric flow response to the land–sea breeze eventually forms a clockwise circulation (the CFCA; Fig. 11d).

The upper-ocean current is mainly driven by surface wind stress, which is proportional to the square of the surface wind. However, the daily mean of the hourly surface wind was used in the daily case. To further explore the contribution of the nonlinearity of wind stress,

that is, the square nature of wind stress, on the dipole-pattern salinity change, we carried out another experiment (called dailyWS case) that is the same as the daily case but uses the daily mean of the hourly wind stress data from the diurnal case. Figure 10d shows the SSS and surface flow differences between the dailyWS and daily case. The pattern of the differences in general agreed well with that between the diurnal and daily cases (Fig. 10c), but with a smaller magnitude. Overall, the nonlinearity effect contributed about a half of the dipole-pattern SSS change and the CFCA caused by the diurnal wind effect (Fig. 10c versus Fig. 10d).

d. The Ekman effect

During the sea breeze, the 90° surface flow deflection relative to the 10-m wind field (Fig. 11c), associated with the clockwise rotating flow profile spiral (Figs. 12a–d),

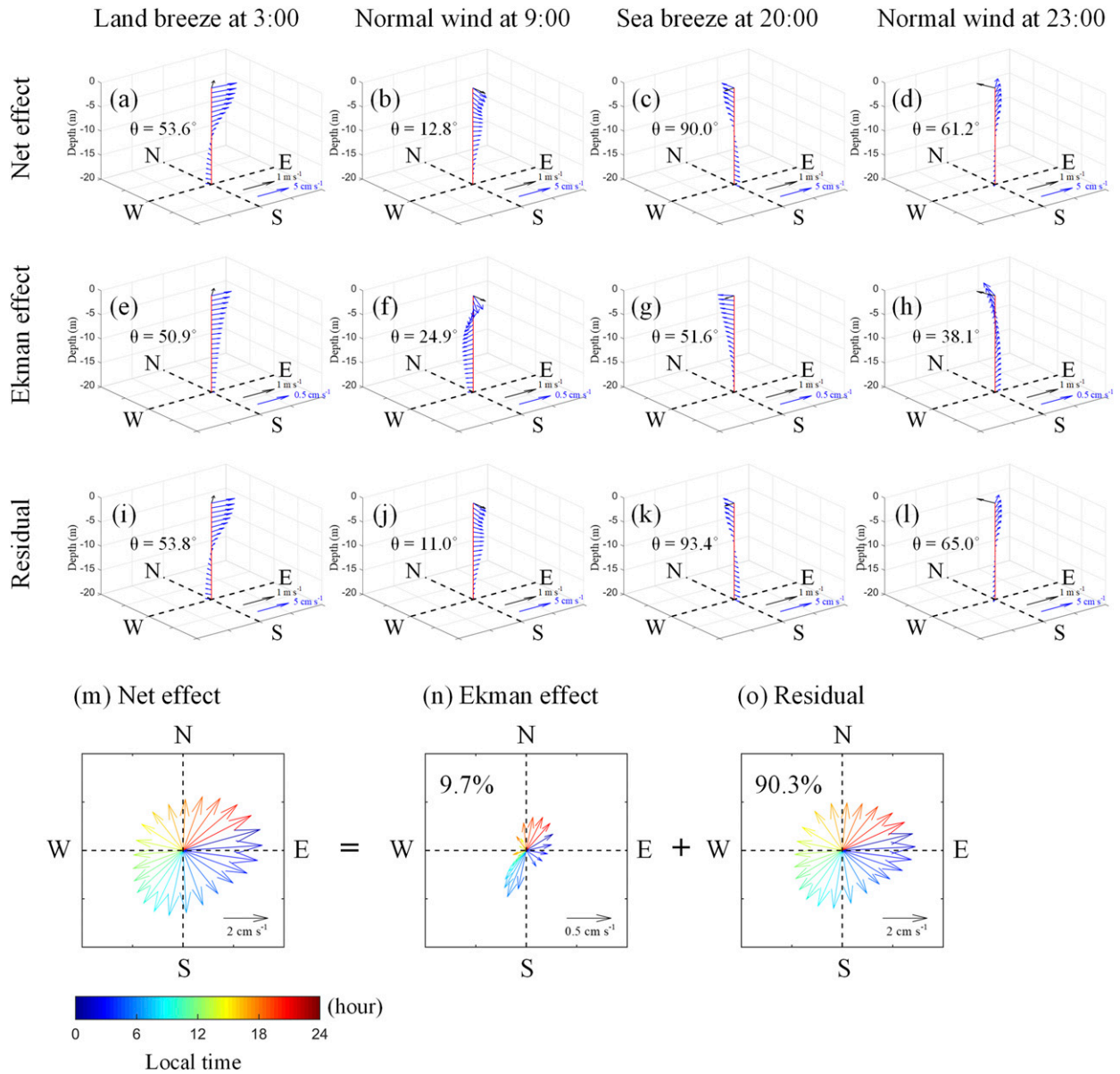


FIG. 12. Regionally averaged 10-m wind (black vectors) and ocean flow (blue vectors) differences between the diurnal case and the daily case over the Yangtze River plume region at local time (a) 0300, (b) 0900, (c) 2000, and (d) 2300 LT in summer (average from May to August over the 5-yr-period model integration); the decomposition of the flow profile into (e)–(h) Ekman effects and (i)–(l) the current residual (original currents minus the Ekman effects); and (m)–(o) the average flow in the mixed layer at different time (local time) of the day. Vector colors in (m)–(o) represent the time during the day. Deflection angle θ is the angle between the 10-m wind and the surface flow; the positive θ means the surface flow is deflected to the right relative to the wind.

suggests that the CFCA response to the land–sea breeze may potentially come from the Ekman effect, that is, due to the Yangtze River plume, the associated low-density surface freshwater enhances stratification and reduces vertical mixing to adjust the Ekman response. Thus, we further examined the Ekman layer effect on the CFCA quantitatively. Following Ekman (1905), the wind-driven Ekman current can be described by the following equations:

$$\frac{\partial u}{\partial t} - fv = \frac{\partial}{\partial z} \left(\mu \frac{\partial u}{\partial z} \right), \quad (7)$$

$$\frac{\partial v}{\partial t} + fu = \frac{\partial}{\partial z} \left(\mu \frac{\partial v}{\partial z} \right), \quad (8)$$

where u and v are eastward and northward Ekman current components, f is the Coriolis frequency, and μ is

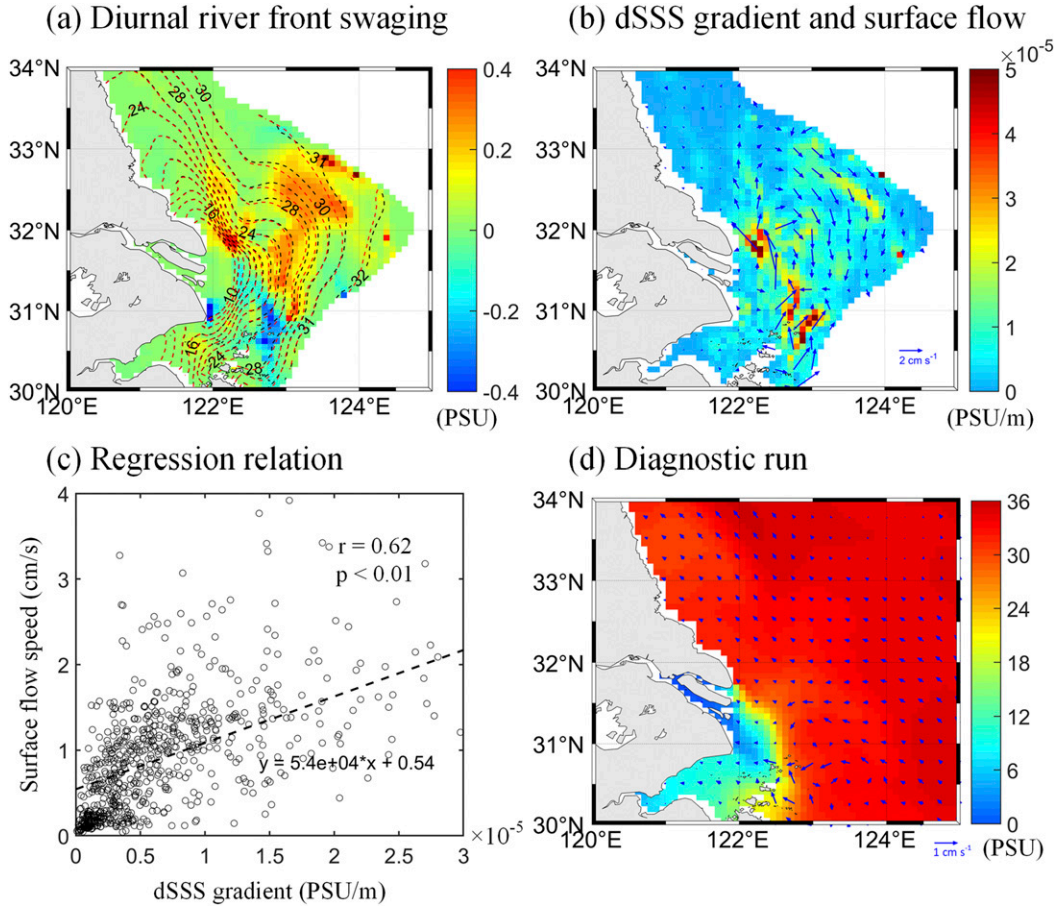


FIG. 13. (a) Distributions of the salinity difference (shading color) between the sea breeze (red dashed line) and land breeze (black dashed line); (b) spatial and (c) regression relations between the horizontal gradient of the day–night salinity difference [salinity at sea breeze minus the salinity at land breeze; shading color in (b) and x -axis data in (c)] and the daily mean flow difference between the diurnal case and the daily case [blue vectors in (b) and y -axis data in (c)]; and (d) background salinity (shading color) and the daily mean flow difference (blue vectors) between the diurnal forcing run and the daily forcing run in diagnostic experiments.

the viscosity coefficient. Under the steady state assumption with the boundary conditions below

$$\mu \frac{\partial u}{\partial z} = \frac{\tau_x}{\rho}, \quad \mu \frac{\partial v}{\partial z} = \frac{\tau_y}{\rho}, \quad \text{at } z = 0, \quad (9)$$

$$u = v = 0, \quad \text{at } z = -D, \quad (10)$$

where τ_x and τ_y are eastward and northward wind stress components, respectively, ρ is water density and D is the water depth, Eqs. (7) and (8) have the following analytical solution:

$$\omega = u + iv = \frac{1}{\sqrt{f\mu}} \frac{|\tau|}{\rho} \exp\left[i\left(\varphi - \frac{\pi}{4}\right)\right] \frac{\sinh\left[(1+i)\frac{z+D}{\delta_f}\right]}{\cosh\left[(1+i)\frac{D}{\delta_f}\right]}, \quad (11)$$

$$\delta_f = \sqrt{\frac{2\mu}{f}}, \quad (12)$$

where ω is the Ekman current; τ is the wind stress and can be expressed as a plural form $\tau = \tau_x + i\tau_y = |\tau|\exp(i\varphi)$, where φ is the wind direction angle and $|\cdot|$ is the absolute norm operator; and δ_f is a critical depth. The critical depth δ_f has a relationship with the Ekman depth (depth of Ekman layer) of $D_E = \pi\delta_f$.

The Ekman effect can be estimated using Eqs. (11) and (12), which were used to derive the Ekman current, directly forced by the surface wind stress. The deflection angle of the diurnal-wind-induced Ekman current relative to the diurnal wind field varied from 24.9° to 51.6° (Figs. 12e–h). However, after removing the Ekman effect, the residual diurnal currents are still similar to the original ones (Figs. 12i–l versus Figs. 12a–d, respectively).

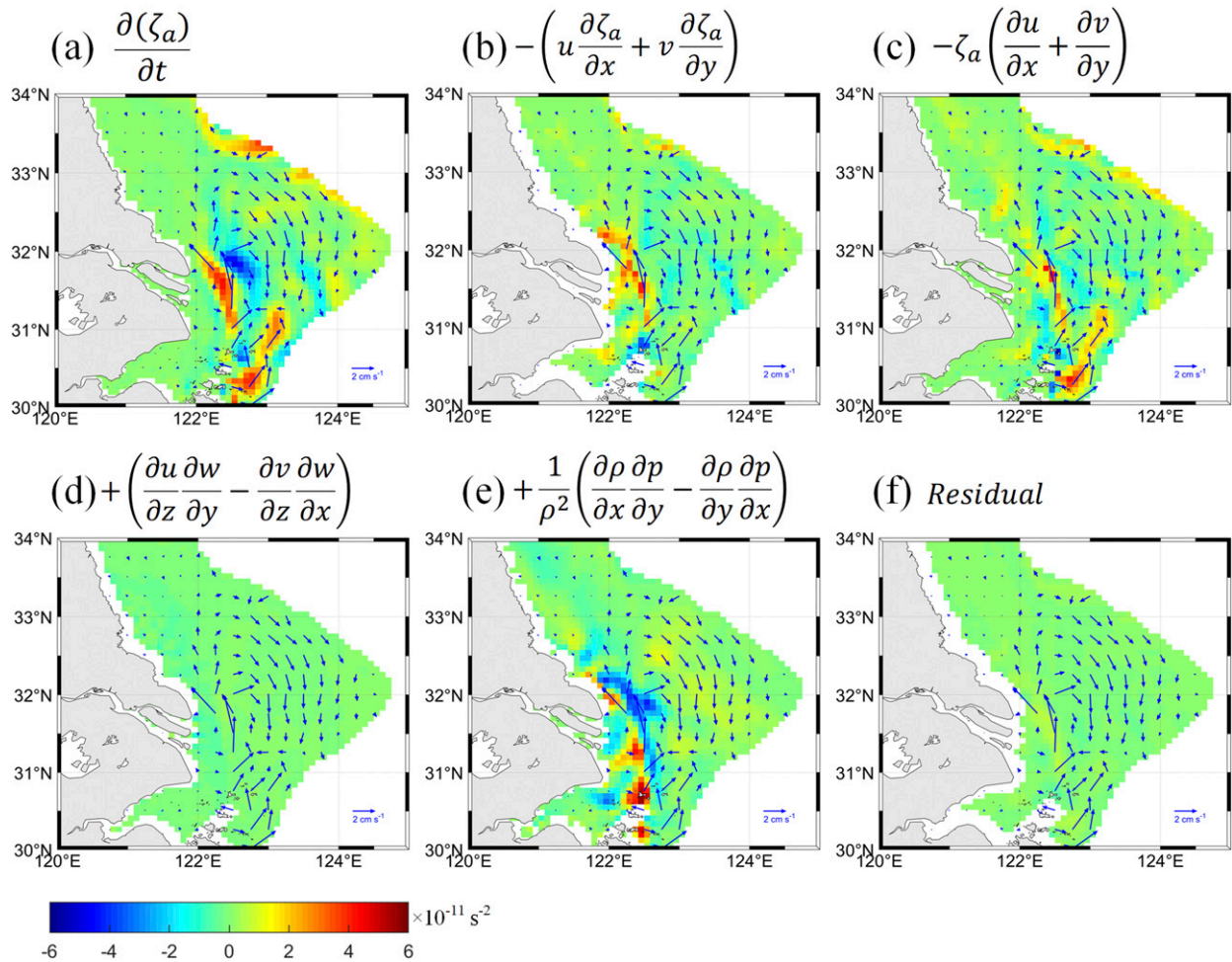


FIG. 14. Differences of (a) the local change rate of the relative vorticity, (b) horizontal advection terms, (c) divergence term, (d) tilting term, (e) solenoidal term, and (f) the residual term between the diurnal case and the daily case.

This is because the derived Ekman current (Figs. 12e–h) is one order smaller than the modeled diurnal current (Figs. 12a–d). We further quantify the contribution of the derived Ekman effect to the total diurnal current effect in the mixed layer, using their u and v components of the flow vector deviations. The derived Ekman effect can count for only 9.7% of the modeled diurnal current, leaving 90.3% to other processes (Figs. 12m–o).

e. Diurnal front swing and baroclinic adjustment

Section 4d indicates that the Ekman effect cannot fully explain the flow changes in the diurnal case. We further diagnosed the potential causes of the CFCA using the vorticity budget. Before this, we analyzed the SSS front variation due to the diurnal winds as it may result in the change of baroclinicity. The land–sea breeze causes the swinging (i.e., day–night variation of isohalines) of the Yangtze River front, producing the SSS

difference (dSSS) between the sea breeze (2000 LT) and the land breeze (0300 LT) (Fig. 13a). The large dSSS gradient showed a similar pattern to the CFCA (Fig. 13b) and the correlation between these two fields was 0.62 ($p < 0.01$; Fig. 13c). An additional sensitivity experiment also confirmed this connection. When the model salinity and temperature were fixed (i.e., the density is fixed) to the model initial conditions (i.e., 0000 UTC 1 January 2011) for both the diurnal and daily cases during the 5-yr integration, the CFCA disappeared with a small differences in the flow field (Fig. 13d). This implies that the SSS variation (the baroclinic adjustment) due to the diurnal winds might be important to the CFCA formation and, in consequence, the dipole pattern of the SSS change.

To further clarify this baroclinic adjustment process, we performed the budget analysis of the vertical component of the vorticity using the following equation:

$$\begin{aligned} \frac{\partial \zeta_a}{\partial t} = & - \left(u \frac{\partial \zeta_a}{\partial x} + v \frac{\partial \zeta_a}{\partial y} \right) - \zeta_a \left(\frac{\partial u}{\partial x} + \frac{\partial v}{\partial y} \right) \\ & + \left(\frac{\partial u}{\partial z} \frac{\partial w}{\partial y} - \frac{\partial v}{\partial z} \frac{\partial w}{\partial x} \right) + \frac{1}{\rho^2} \left(\frac{\partial \rho}{\partial x} \frac{\partial p}{\partial y} - \frac{\partial \rho}{\partial y} \frac{\partial p}{\partial x} \right) \\ & + \text{residual}, \end{aligned} \quad (13)$$

where $\zeta_a = \zeta + f$ is the vertical component of the absolute vorticity; $\zeta = [(\partial v/\partial x) - (\partial u/\partial y)]$ the relative vorticity; f the planetary vorticity; u , v , and w the eastward, northward, and vertical current components, respectively; ρ the density; and p the pressure derived from the hydrostatic balance relation ($p = \rho g z$). The left-hand side of Eq. (13) is the local change rate (or tendency) of the relative vorticity. The terms, in sequence, on the right-hand side are the horizontal advection, divergence, tilting, solenoidal (or baroclinic) and residual, respectively.

Figure 14 shows the May–August differences of vorticity budget terms between the diurnal case and the daily case over the 5-yr simulation. The vorticity tendency differences between these two experiments show a positive and negative pair of vorticities change offshore of the Yangtze River estuary (Fig. 14a), which can explain the northwestward jetlike current difference. This pair of vorticity change induces the jetlike current anomaly between these two vorticity anomalies, thus transporting more freshwater to the south of Jiangsu Coast, where the northward current along Jiangsu Coast (driven by both tides and winds in summer) carries more freshwater to the entire Jiangsu coastal waters. The jetlike current thus enhances the NLFT of freshwater (also means less freshwater transport east-northeastward), forming the dipole pattern of SSS change (Figs. 10c and 14a). The positive change in the vorticity tendency dipole (Fig. 14a) is mainly caused by the advection term (Fig. 14b) with the aid of divergence term (Fig. 14c), and the negative change comes mostly from the solenoidal (baroclinicity) term (Fig. 14e). The tilting (Fig. 14d) and residual terms (Fig. 14f) have little contribution to the vorticity tendency difference and thus can be ignored. This vorticity tendency difference can be explained by the compensation between the baroclinicity and advection terms. As the fresh river water flows into the ocean, the baroclinicity may be generated from the frontal jet, causing the negative vorticity tendency on the light side of the front due to the compression (Figs. 10a,b). Our results suggest more baroclinicity is generated in the diurnal case than in the daily case, leading to a more negative vorticity tendency along the front. The northward migration (advection) of the river front and the stronger compression of

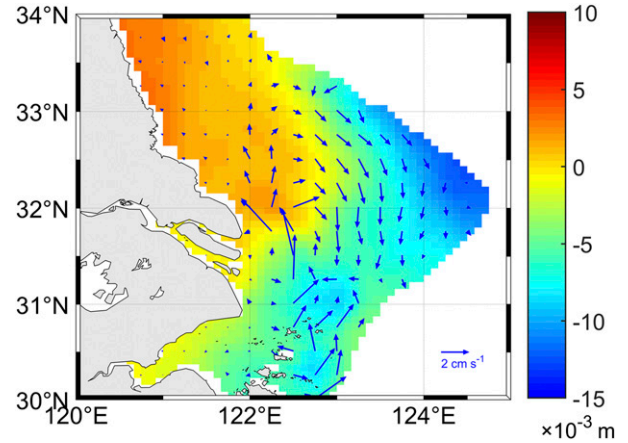


FIG. 15. Distribution of summer (average from May to August over the 5-yr-period model simulation) SSH and surface flow differences between the diurnal case and the daily case. Shaded colors indicate the SSH difference, and the blue vectors represent the flow field difference between the two cases.

baroclinicity lead to the observed pair of vorticity change.

However, the change of outer part current of the CFCA is caused by a different mechanism. The jetlike current, induced by the diurnal forcing, transports more Yangtze River freshwater northwestward along Jiangsu Coast in summer and increases the mean (May–August) SSH over the region (Fig. 15). The enhanced NLFT induced by the diurnal wind weakens the northeastward Yangtze River freshwater transport branch and reduces the mean SSH in the northeast of the Yangtze River plume region. Therefore, an SSH gradient appears and forms the outer part current of CFCA through the geostrophic adjustment (Fig. 15).

5. Sensitivity to forcing frequency

We carried out three additional sensitivity experiments to examine the influence of surface wind forcing frequency on the dipole-pattern salinity change induced by the diurnal wind. The three experiments were conducted using different frequencies of surface wind forcing: 3 hourly (3H), 6 hourly (6H), and 12 hourly (12H). All other setups are exactly the same as those of the diurnal and daily cases.

During May–August, similar dipole pattern of salinity change (deviated from the daily case) also appeared in all these experiments (Figs. 16b–d). The strength of this dipole pattern of salinity change grew with the increased forcing frequency (Fig. 16). Specifically, the 3H case almost reproduced the dipole pattern of the salinity change in the diurnal case (Figs. 16a,b). This implies that a minimum of 3-hourly wind frequency

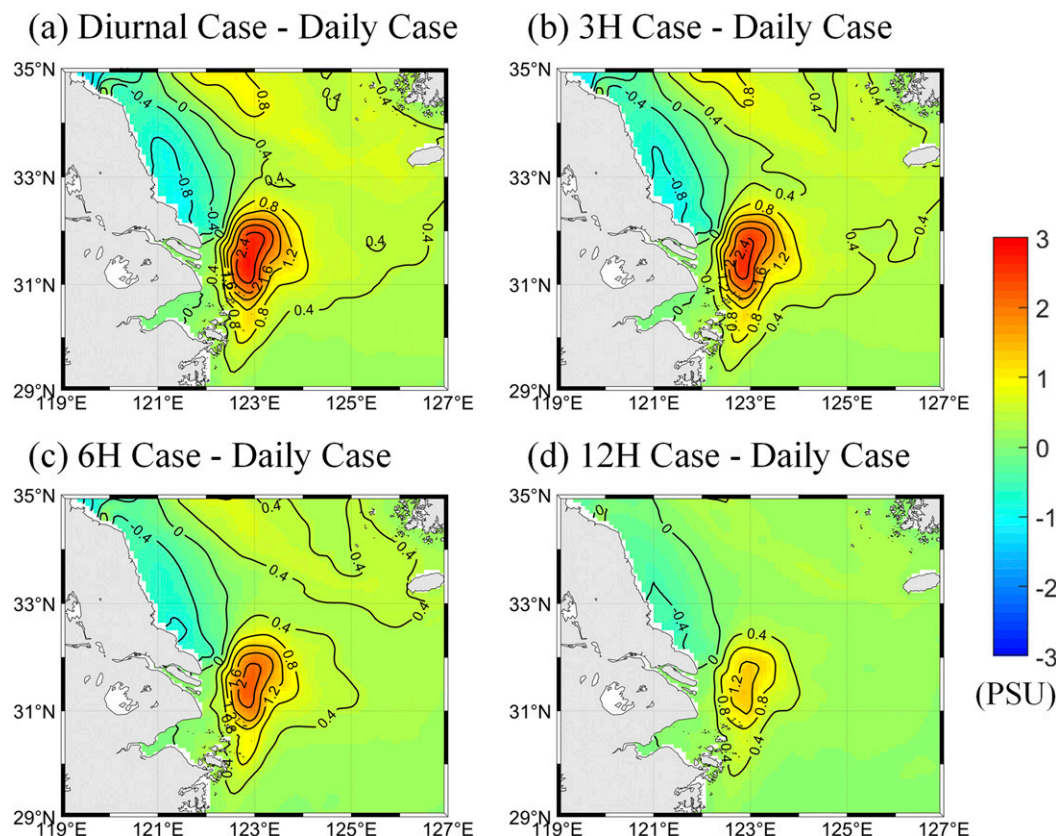


FIG. 16. Summer (May–August) SSS difference between different time interval simulation groups (a) diurnal case – daily case, (b) 3H case – daily case, (c) 6H case – daily case, and (d) 12H case – daily case.

is required to accurately simulate the oceanic response of the diurnal forcing, a similar conclusion obtained in [Qu and Hetland \(2019\)](#). However, our results suggest that both the direct influence of wind kinetic energy input, proposed by [Hunter et al. \(2010\)](#) and [Qu and Hetland \(2019\)](#), and the baroclinic adjustment process (as discussed in [section 4](#)) are essential for this dipole pattern salinity change.

6. Conclusions

This study investigates the impacts of diurnal atmospheric forcing on the summer salinity change in the ECS. A moderate-resolution ROMS model was forced respectively by the hourly and daily ECMWF ERA5 reanalysis data from 2011 to 2015. Compared with a daily frequency forcing experiment (the daily case), the hourly atmospheric forcing (the diurnal case) increased the salinity by 1–2 psu outside of the Yangtze River estuary and decreased by 0.5–1 psu in the Jiangsu Coast, causing a dipole pattern of salinity change in the ECS. Dye tracking experiments confirm that the diurnal forcing transported more Yangtze River freshwater

northwestward along the Jiangsu Coast, rather than heading northeastward in summer. The volume of NLFT was increased by $5.2 \times 10^9 \text{ m}^3$ and the mean water age was reduced by 7 days.

Further sensitivity experiments, using diurnal wind or diurnal insolation, suggest that the wind field was the most effective factor contributing to the dipole pattern of the salinity difference and the large changes in the NLFT. The diurnal wind, that is, the land–sea breeze, produced a diurnal swing of Yangtze River freshwater front, which then formed a CFCA outside of the Yangtze River estuary through baroclinic adjustment. This CFCA was responsible for the summertime dipole pattern of the salinity difference between the diurnal case and the daily case; it hindered the northeastward offshore freshwater transport of Yangtze River and strengthened the NLFT in summer.

This study demonstrates that diurnal forcing can modulate long-term material transport in the ECS, although diurnal atmospheric forcing only contributed 5% to the mean volume of NLFT in summer ([Table 2](#) and [Fig. 7c](#)). The enhanced NLFT and the dipole pattern of salinity difference are clearly shown in the 5-yr model

simulations (Fig. 8). A 1-psu salinity change may have great impacts on the marine ecosystem (Doney et al. 2011; Hoegh-Guldberg and Bruno 2010). In this respect, diurnal forcing can be very important to the high-ecological-activity marginal seas at midlatitudes, such as the ECS.

Furthermore, we explored the sensitivity of the wind forcing frequency to the dipole pattern formation of the salinity change. A 3-hourly wind can reproduce this summer dipole pattern of salinity change in the ECS. Though our results are similar to the conclusion suggested by Qu and Hetland (2019), we noticed that the mechanism behind this results from both the direct kinetic energy input and the baroclinic adjustment induced by the diurnal winds.

Acknowledgments. This work was supported by NSFC-Shandong Joint Fund for Marine Ecology and Environmental Sciences (U1606404) and the Youth Foundation of Shandong Academy of Sciences (2019QN0026). Y. Yu thanks the China Scholarship Council (CSC) for supporting his stay in the United States. We thank Prof. Wensheng Jiang in Ocean University of China for providing the cruise data. The buoy data were collected via a research project funded by the Ocean Public Welfare Scientific Research Project, State Oceanic Administration People's Republic of China through Grant 200905012 (subtask 200905012-6). The authors are very grateful to two anonymous reviewers for their constructive comments and suggestions.

REFERENCES

- Anderson, S. P., R. A. Weller, and R. B. Lukas, 1996: Surface buoyancy forcing and the mixed layer of the Western Pacific warm pool: Observations and 1D model results. *J. Climate*, **9**, 3056–3085, [https://doi.org/10.1175/1520-0442\(1996\)009<3056:SBFATM>2.0.CO;2](https://doi.org/10.1175/1520-0442(1996)009<3056:SBFATM>2.0.CO;2).
- Beardsley, R. C., R. Limeburner, H. Yu, and G. A. Cannon, 1985: Discharge of the Changjiang (Yangtze River) into the East China Sea. *Cont. Shelf Res.*, **4**, 57–76, [https://doi.org/10.1016/0278-4343\(85\)90022-6](https://doi.org/10.1016/0278-4343(85)90022-6).
- Berliand, M. E., 1952: Determining the net long-wave radiation of the earth with consideration of the effect of cloudiness. *Izv. Akad. Nauk SSSR, Ser. Geofiz.*, **1**, 64–78.
- Bernie, D. J., S. J. Woolnough, J. M. Slingo, and E. Guilyardi, 2005: Modeling diurnal and intraseasonal variability of the ocean mixed layer. *J. Climate*, **18**, 1190–1202, <https://doi.org/10.1175/JCLI3319.1>.
- , and Coauthors, 2007: Impact of resolving the diurnal cycle in an ocean–atmosphere GCM. Part 1: A diurnally forced OGCM. *Climate Dyn.*, **29**, 575–590, <https://doi.org/10.1007/s00382-007-0249-6>.
- Carton, J. A., G. A. Chepurin, and L. Chen, 2018: SODA3: A new ocean climate reanalysis. *J. Climate*, **31**, 6967–6983, <https://doi.org/10.1175/JCLI-D-18-0149.1>.
- Chang, P., and A. Isobe, 2003: A numerical study on the Changjiang diluted water in the Yellow and East China Seas. *J. Geophys. Res.*, **108**, 3299, <https://doi.org/10.1029/2002JC001749>.
- Copernicus Climate Change Service, 2017: ERA5: Fifth generation of ECMWF atmospheric reanalyses of the global climate. Copernicus Climate Change Service Climate Data Store, <https://cds.climate.copernicus.eu/cdsapp#!/home>.
- Cronin, M. F., and M. J. McPhaden, 1999: Diurnal cycle of rainfall and surface salinity in the Western Pacific warm pool. *Geophys. Res. Lett.*, **26**, 3465–3468, <https://doi.org/10.1029/1999GL010504>.
- Deleersnijder, E., J. M. Campin, and E. J. M. Delhez, 2001: The concept of age in marine modelling: I. Theory and preliminary model results. *J. Mar. Syst.*, **28**, 229–267, [https://doi.org/10.1016/S0924-7963\(01\)00026-4](https://doi.org/10.1016/S0924-7963(01)00026-4).
- Delhez, E. J. M., J. M. Campin, A. C. Hirst, and E. Deleersnijder, 1999: Toward a general theory of the age in ocean modelling. *Ocean Modell.*, **1**, 17–27, [https://doi.org/10.1016/S1463-5003\(99\)00003-7](https://doi.org/10.1016/S1463-5003(99)00003-7).
- Doney, S. C., and Coauthors, 2011: Climate change impacts on marine ecosystems. *Annu. Rev. Mar. Sci.*, **4**, 11–37, <https://doi.org/10.1146/ANNUREV-MARINE-041911-111611>.
- Drushka, K., S. T. Gille, and J. Sprintall, 2014: The diurnal salinity cycle in the tropics. *J. Geophys. Res. Oceans*, **119**, 5874–5890, <https://doi.org/10.1002/2014JC009924>.
- Egbert, G. D., and S. Y. Erofeeva, 2002: Efficient inverse modeling of barotropic ocean tides. *J. Atmos. Oceanic Technol.*, **19**, 183–204, [https://doi.org/10.1175/1520-0426\(2002\)019<0183:EIMOBO>2.0.CO;2](https://doi.org/10.1175/1520-0426(2002)019<0183:EIMOBO>2.0.CO;2).
- , A. F. Bennett, and M. G. G. Foreman, 1994: TOPEX/Poseidon tides estimated using a global inverse model. *J. Geophys. Res.*, **99**, 24 821–24 852, <https://doi.org/10.1029/94JC01894>.
- Ekman, V. W., 1905: On the influence of the earth's rotation on ocean-currents. *Ark. Mat. Astron. Fys.*, **2**, 1–53.
- Fairall, C. W., E. F. Bradley, J. S. Godfrey, G. A. Wick, J. B. Edson, and G. S. Young, 1996a: Cool-skin and warm-layer effects on sea surface temperature. *J. Geophys. Res.*, **101**, 1295–1308, <https://doi.org/10.1029/95JC03190>.
- , —, D. P. Rogers, J. B. Edson, and G. S. Young, 1996b: Bulk parameterization of air-sea fluxes for tropical ocean-global atmosphere coupled-ocean atmosphere response experiment. *J. Geophys. Res.*, **101**, 3747–3764, <https://doi.org/10.1029/95JC03205>.
- , —, J. E. Hare, A. A. Grachev, and J. B. Edson, 2003: Bulk parameterization of air-sea fluxes: Updates and verification for the COARE algorithm. *J. Climate*, **16**, 571–591, [https://doi.org/10.1175/1520-0442\(2003\)016<0571:BPOASF>2.0.CO;2](https://doi.org/10.1175/1520-0442(2003)016<0571:BPOASF>2.0.CO;2).
- Fine, E. C., F. O. Bryan, W. G. Large, and D. A. Bailey, 2015: An initial estimate of the global distribution of diurnal variation in sea surface salinity. *J. Geophys. Res. Oceans*, **120**, 3211–3228, <https://doi.org/10.1002/2014JC010483>.
- Hodges, B. A., and D. M. Fratantoni, 2014: AUV observations of the diurnal surface layer in the North Atlantic salinity maximum. *J. Phys. Oceanogr.*, **44**, 1595–1604, <https://doi.org/10.1175/JPO-D-13-0140.1>.
- Hoegh-Guldberg, O., and J. F. Bruno, 2010: The impact of climate change on the world's marine ecosystems. *Science*, **328**, 1523–1528, <https://doi.org/10.1126/SCIENCE.1189930>.
- Huang, M., Z. Gao, S. Miao, and X. Xu, 2016: Characteristics of sea breezes over the Jiangsu coastal area, China. *Int. J. Climatol.*, **36**, 3908–3916, <https://doi.org/10.1002/joc.4602>.
- Hunter, E. J., R. Chant, L. Bowers, S. Glenn, and J. Kohut, 2007: Spatial and temporal variability of diurnal wind forcing in the

- coastal ocean. *Geophys. Res. Lett.*, **34**, L03607, <https://doi.org/10.1029/2006GL028945>.
- , R. J. Chant, J. L. Wilkin, and J. Kohut, 2010: High-frequency forcing and subtidal response of the Hudson River plume. *J. Geophys. Res.*, **115**, C07012, <https://doi.org/10.1029/2009JC005620>.
- Kako, S., T. Nakagawa, K. Takayama, N. Hirose, and A. Isobe, 2016: Impact of Changjiang River discharge on sea surface temperature in the East China Sea. *J. Phys. Oceanogr.*, **46**, 1735–1750, <https://doi.org/10.1175/JPO-D-15-0167.1>.
- Kalnay, E., and Coauthors, 1996: The NCEP/NCAR 40-Year Reanalysis Project. *Bull. Amer. Meteor. Soc.*, **77**, 437–471, [https://doi.org/10.1175/1520-0477\(1996\)077<0437:TNYRP>2.0.CO;2](https://doi.org/10.1175/1520-0477(1996)077<0437:TNYRP>2.0.CO;2).
- Kim, H. C., and Coauthors, 2009: Distribution of Changjiang diluted water detected by satellite chlorophyll-a and its interannual variation during 1998–2007. *J. Oceanogr.*, **65**, 129–135, <https://doi.org/10.1007/s10872-009-0013-0>.
- Lie, H. J., C. H. Cho, J. H. Lee, and S. Lee, 2003: Structure and eastward extension of the Changjiang River plume in the East China Sea. *J. Geophys. Res.*, **108**, 3077, <https://doi.org/10.1029/2001JC001194>.
- Lin, Y., and Coauthors, 2019: Characteristics and simulation biases of corkscrew sea breezes on the East Coast of China. *J. Geophys. Res. Atmos.*, **124**, 18–34, <https://doi.org/10.1029/2017JD028163>.
- Lukas, R., and E. Lindstrom, 1991: The mixed layer of the western equatorial Pacific Ocean. *J. Geophys. Res.*, **96**, 3343–3357, <https://doi.org/10.1029/90JC01951>.
- Mao, H., Z. Gan, and S. Lan, 1963: Preliminary study on the Changjiang diluted water and its mixing natures. *Oceanol. Limnol. Sin.*, **5**, 183–206.
- Mellor, G. L., and T. Yamada, 1982: Development of a turbulent closure model for geophysical fluid problems. *Rev. Geophys. Space Phys.*, **20**, 851–875, <https://doi.org/10.1029/RG020i004p00851>.
- Ministry of Water Resources, 2011: Chinese River Sediment Bulletin. Ministry of Water Resources of the People's Republic of China, <http://www.mwr.gov.cn/sj/tjgb/zghlnsgb/>.
- , 2012: Chinese River Sediment Bulletin. Ministry of Water Resources of the People's Republic of China, <http://www.mwr.gov.cn/sj/tjgb/zghlnsgb/>.
- , 2013: Chinese River Sediment Bulletin. Ministry of Water Resources of the People's Republic of China, <http://www.mwr.gov.cn/sj/tjgb/zghlnsgb/>.
- , 2014: Chinese River Sediment Bulletin. Ministry of Water Resources of the People's Republic of China, <http://www.mwr.gov.cn/sj/tjgb/zghlnsgb/>.
- , 2015: Chinese River Sediment Bulletin. Ministry of Water Resources of the People's Republic of China, <http://www.mwr.gov.cn/sj/tjgb/zghlnsgb/>.
- Montégut, C. D. B., J. Mignot, A. Lazar, and S. Cravatte, 2007: Control of salinity on the mixed layer depth in the world ocean: 1. General description. *J. Geophys. Res.*, **112**, C06011, <https://doi.org/10.1029/2006JC003953>.
- Moon, J.-H., I.-C. Pang, and J.-H. Yoon, 2009: Response of the Changjiang diluted water around Jeju Island to external forcings: A modeling study of 2002 and 2006. *Cont. Shelf Res.*, **29**, 1549–1564, <https://doi.org/10.1016/j.csr.2009.04.007>.
- , N. Hirose, J.-H. Yoon, and I.-C. Pang, 2010: Offshore detachment process of the low-salinity water around Changjiang bank in the East China Sea. *J. Phys. Oceanogr.*, **40**, 1035–1053, <https://doi.org/10.1175/2010JPO4167.1>.
- Paulson, C. A., and J. J. Simpson, 1977: Irradiance measurements in the upper ocean. *J. Phys. Oceanogr.*, **7**, 952–956, [https://doi.org/10.1175/1520-0485\(1977\)007<0952:IMITUO>2.0.CO;2](https://doi.org/10.1175/1520-0485(1977)007<0952:IMITUO>2.0.CO;2).
- Pawlowicz, R., B. Beardsley, and S. Lentz, 2002: Classical tidal harmonic analysis including error estimates in MATLAB using T_TIDE. *Comput. Geosci.*, **28**, 929–937, [https://doi.org/10.1016/S0098-3004\(02\)00013-4](https://doi.org/10.1016/S0098-3004(02)00013-4).
- Piñones, A., A. Valle-Levinson, D. A. Narváez, C. A. Vargas, S. A. Navarrete, G. Yuras, and J. C. Castilla, 2005: Wind-induced diurnal variability in river plume motion. *Estuarine Coastal Shelf Sci.*, **65**, 513–525, <https://doi.org/10.1016/j.ecss.2005.06.016>.
- Price, J. F., R. A. Weller, and R. Pinkel, 1986: Diurnal cycling: Observations and models of the upper ocean response to diurnal heating, cooling, and wind mixing. *J. Geophys. Res.*, **91**, 8411–8427, <https://doi.org/10.1029/JC091iC07p08411>.
- Qu, L., and R. D. Hetland, 2019: Temporal resolution of wind forcing required for river plume simulations. *J. Geophys. Res. Oceans*, **124**, 1459–1473, <https://doi.org/10.1029/2018JC014593>.
- Quan, Q., X. Mao, X. Yang, H. U. Yingying, H. Zhang, and W. Jiang, 2013: Seasonal variations of several main water masses in the Southern Yellow Sea and East China Sea in 2011. *J. Ocean Univ. China*, **12**, 524–536, <https://doi.org/10.1007/s11802-013-2198-5>.
- Reynolds-Fleming, J. V., and R. A. Luettich, 2004: Wind-driven lateral variability in a partially mixed estuary. *Estuarine Coastal Shelf Sci.*, **60**, 395–407, <https://doi.org/10.1016/j.ecss.2004.02.003>.
- Rong, Z., and M. Li, 2012: Tidal effects on the bulge region of Changjiang River plume. *Estuarine Coastal Shelf Sci.*, **97**, 149–160, <https://doi.org/10.1016/j.ecss.2011.11.035>.
- Senjyu, T., H. Enomoto, T. Matsuno, and S. Matsui, 2006: Interannual salinity variations in the Tsushima Strait and its relation to the Changjiang discharge. *J. Oceanogr.*, **62**, 681–692, <https://doi.org/10.1007/s10872-006-0086-y>.
- Shchepetkin, A. F., and J. C. McWilliams, 2005: The Regional Oceanic Modeling System (ROMS): A split-explicit, free-surface, topography-following-coordinate oceanic model. *Ocean Modell.*, **9**, 347–404, <https://doi.org/10.1016/j.ocemod.2004.08.002>.
- , and —, 2009: Correction and commentary for “Ocean forecasting in terrain-following coordinates: Formulation and skill assessment of the regional ocean modeling system” by Haidvogel et al., *J. Comp. Phys.* 227, pp. 3595–3624. *J. Comput. Phys.*, **228**, 8985–9000, <https://doi.org/10.1016/j.jcp.2009.09.002>.
- Shen, H., C. Zhang, C. Xiao, and J. Zhu, 1998: Change of the discharge and sediment flux to estuary in the Changjiang River. *Health of the Yellow Sea*, G. H. Hong, J. Zhang, and B. K. Park, Eds., Earth Love, 129–148.
- Shi, J. Z., and L.-F. Lu, 2011: A short note on the dispersion, mixing, stratification and circulation within the plume of the partially-mixed Changjiang River estuary, China. *J. Hydro-Environ. Res.*, **5**, 111–126, <https://doi.org/10.1016/j.jher.2010.06.002>.
- Smagorinsky, J., 1963: General circulation experiments with the primitive equations. *Mon. Wea. Rev.*, **91**, 99–164, [https://doi.org/10.1175/1520-0493\(1963\)091<0099:GCEWTP>2.3.CO;2](https://doi.org/10.1175/1520-0493(1963)091<0099:GCEWTP>2.3.CO;2).
- Soloviev, A., and R. Lukas, 2006: *The Near-Surface Layer of the Ocean*. Springer, 572 pp.
- Su, Y. S., and X. C. Weng, 1994: Water masses in China seas. *Oceanology of the East China Seas*, Di et al., Eds., Kluwer Academic, 3–16.
- Sverdrup, H. U., M. W. Johnson, and R. H. Fleming, 1942: *The Oceans, Their Physics, Chemistry, and General Biology*. Prentice-Hall, Inc., 1087 pp.
- Thomson, R. E., and I. V. Fine, 2003: Estimating mixed layer depth from oceanic profile data. *J. Atmos. Oceanic Technol.*,

- 20, 319–329, [https://doi.org/10.1175/1520-0426\(2003\)020<0319:EMLDFO>2.0.CO;2](https://doi.org/10.1175/1520-0426(2003)020<0319:EMLDFO>2.0.CO;2).
- Thushara, V., and P. N. Vinayachandran, 2014: Impact of diurnal forcing on intraseasonal sea surface temperature oscillations in the Bay of Bengal. *J. Geophys. Res. Oceans*, **119**, 8221–8241, <https://doi.org/10.1002/2013JC009746>.
- Vorosmarty, C. J., B. M. Fekete, and B. A. Tucker, 1998: Global river discharge, 1807–1991, version 1.1 (RivDIS). Oak Ridge National Laboratory Distributed Active Archive Center, accessed 2 August 2015, <http://doi.org/10.3334/ORNLDAAC/199>.
- Wang, Y., J. Shen, Q. He, L. Zhu, and D. Zhang, 2015: Seasonal variations of transport time of freshwater exchanges between Changjiang Estuary and its adjacent regions. *Estuarine Coastal Shelf Sci.*, **157**, 109–119, <https://doi.org/10.1016/j.ecss.2015.03.008>.
- Wohl, E. E., 2008: Hydrology and discharge. *Large Rivers: Geomorphology and Management*, A. Gupta, Ed., John Wiley & Sons, 29–44.
- Wu, H., J. Zhu, J. Shen, and H. Wang, 2011: Tidal modulation on the Changjiang River plume in summer. *J. Geophys. Res.*, **116**, C08017, <https://doi.org/10.1029/2011JC007209>.
- , J. Shen, J. Zhu, J. Zhang, and L. Li, 2014: Characteristics of the Changjiang plume and its extension along the Jiangsu Coast. *Cont. Shelf Res.*, **76**, 108–123, <https://doi.org/10.1016/j.csr.2014.01.007>.
- , T. Wu, J. Shen, and J. Zhu, 2018: Dynamics of the Changjiang River Plume. *Coastal Environment, Disaster, and Infrastructure: A case Study of China's Coastline*, X. San Liang and Y. Zhang, Eds., InTechOpen, 296 pp.
- Yu, Y., H. Gao, J. Shi X. Guo, and G. Liu, 2017: Diurnal forcing induces variations in seasonal temperature and its rectification mechanism in the eastern shelf seas of China. *J. Geophys. Res. Oceans*, **122**, 9870–9888, <https://doi.org/10.1002/2017JC013473>.
- Zhang, X., D. C. Smith, S. F. Dimarco, and R. D. Hetland, 2010: A numerical study of sea-breeze-driven ocean Poincare wave propagation and mixing near the critical latitude. *J. Phys. Oceanogr.*, **40**, 48–66, <https://doi.org/10.1175/2009JPO4216.1>.
- Zhu, J., Y. Li, and H. Shen, 1997: Numerical simulation of the wind field's impact on the expansion of the Changjiang River diluted water in summer. *Oceanol. Limnol. Sin.*, **28**, 34–44.
- Zhu, P., and H. Wu, 2018: Origins and transports of the low-salinity coastal water in the southwestern Yellow Sea. *Acta Oceanol. Sin.*, **37**, 1–11, <https://doi.org/10.1007/s13131-018-1200-x>.